TITLE: Single-Step Synthesis of Shaped Polymeric Particles using Initiated Chemical Vapor Deposition in Liquid Crystals

Short Title: Synthesis Pathway of Shaped Polymeric Particles

Authors: Apoorva Jain[1],† Soumyamouli Pal[1],† Shiqi Li[1], Nicholas L. Abbott[1]*, Rong Yang[1]*

† these authors contributed equally

[1] Robert Frederick Smith School of Chemical and Biomolecular Engineering, Cornell University

Keywords: iCVD, LC-templated polymerization, shaped particles, real-time monitoring, single-step synthesis

Abstract:

We elucidate a synthesis pathway that leads to polymeric nanospheres, orientation-controlled microgels, or microspheroids via single-step polymerization of divinylbenzene (DVB) using initiated chemical vapor deposition (iCVD) in liquid crystals (LC). iCVD supplies vapor-phase reactants continuously, avoiding the critical limitation of reactants disrupting LC structure that plagues past LC-templated polymerization. LC is leveraged as a real-time display of the polymerization conditions and particle emergence, captured using an in-situ long-focal range microscope. Detailed image analysis unravels key LC-guided mechanisms during polymerization. pDVB forms nanospheres due to poor solubilization by nematic LC. The nanospheres partition to the LC-solid interface and further assemble into microgel clusters whose orientation is guided by the LC molecular alignment. On further polymerization,

microgel clusters transition to microspheroids that resemble liquid drops. We identify key energetic factors that guide trajectories along the synthesis pathway, providing the fundamental basis of a framework for engineering particle synthesis with shape control.

Teaser: A synthesis pathway is revealed for shaped particles by continuous polymerization in templating liquid crystals.

MAIN TEXT:

INTRODUCTION

Polymer microparticles have achieved an enormous impact on the global economy, with applications ranging from drug delivery in oncology (*1*) to enabling precision separations in chromatography (*2–4*). Recent fundamental advances have further revealed how particle shape determines their packing and assembly, pointing to metamaterials with reconfigurable structures and programmable dynamic behaviors (*5*, *6*), and how shape dictates the fate of microparticles in a human body (*7–12*). The need for shape-controlled polymer particles has spurred the rapid development of new synthesis approaches, ranging from microfluidic devices (*13*, *14*), to seeded emulsion polymerization (*15*, *16*), to particle replication in non-wetting templates (PRINT) (*17*), to mechanical stretching (*18–24*). While these techniques have led to exciting new shapes, their shape formation fundamentally relies on physical manipulations, which are laborious and hard to scale. There have been few fresh conceptual advances beyond emulsion polymerization and physical manipulation in achieving shape control in recent years.

Take poly(divinylbenzene) (pDVB) microspheres as an example, the synthesis of which has been extensively studied in precipitation polymerization (*25*), owing to its commercial use

as chromatographic packing beads. As unveiled by Stover et al (*26–32*), pDVB microspheres form under marginal solvency, via a 5-step growth mechanism. Starting with a solution of DVB monomers in a marginal solvent (e.g., acetonitrile), oligomeric polymer chains form upon initiation of polymerization, which then aggregate into colloidally-stable microgel nuclei as polymerization proceeds. The microgel nuclei eventually phase separate as solid microparticles and grow further by capturing oligomeric chains through pendant vinyl bonds at their surfaces. The final size is controlled by the solution composition (e.g., concentrations of monomer and initiator) and typically falls in the range of 3 – 5 μm (*32*). The as-formed microparticles are uniformly spherical due to the dominance of surface tension during the phase separation in solution.

Here, we report a framework for the synthesis of shape-controlled polymer particles in liquid crystals (LC), one that is based on the discovery that DVB polymerization occurs at two distinct locations in an anisotropic solvent. Our work builds upon the exciting finding that LCs, with both fluidity and long-range order, can simultaneously serve as a solvent and a template during polymerization. The templating effect gives rise to anisotropic polymeric networks (*33–36*) and oriented nanofibers (*37–39*). While the long-range order directs shape formation, the elastic properties of LC are proposed to influence the sizes of the polymeric structures. Nevertheless, the molecular mechanisms that led to the striking morphologies obtained in LC remain elusive, limiting the capability to rationally design polymeric structures using structured liquids as templates.

This report bridges that knowledge gap by establishing effective real-time monitoring of the microscopic progression of polymerization, leveraging the optical output inherent to LC as indicators of the reacting microenvironment, and the continuous delivery of reactants enabled by initiated Chemical Vapor Deposition (iCVD) (**Figure 1**A-B). Drawing inspiration from the reaction mechanism of precipitation polymerization under marginal solvency, we reveal that

polymer morphologies emerge from a two-stage growth pathway, each resembling the growth mechanism identified by Stover but at different locations in the LC (Figure 1D). In bulk LC, the polymerization yields phase-separated nanospheres in the size range of 160 ± 80 nm. Upon partitioning to the LC-substrate interface, the nanospheres assemble while capturing monomer/oligomers via heterogenous polymerization to form microgel clusters. The aspect ratio and orientation of the clusters are directed by the anisotropic elastic stress of the LC templates near that interface. Upon further aggregation/polymerization, micron-sized spheres and dome-shaped particles emerge from the clusters via surface-tension-driven phase separation. These insights into the mechanism of particle shape formation in LCs enable precise control over the polymer morphology, expanding it from polymeric networks (*40–43*) and nanofibers (*38*, *39*, *44*) to discrete nano/microparticles with sizes and shapes that emerge from an interplay of interfacial energy, elastic energy and dynamic properties of the LC. The reported approach could lead to drug delivery systems with programmable pharmacokinetics (*45–47*) and targeting effects or self-propelled microrockets with controlled group behaviors (*48*). The fundamental insights obtained in this work have the potential to inform the development of unprecedented synthesis mechanisms, applicable to precipitation polymerization, emulsion polymerization, and other solution polymerization approaches.

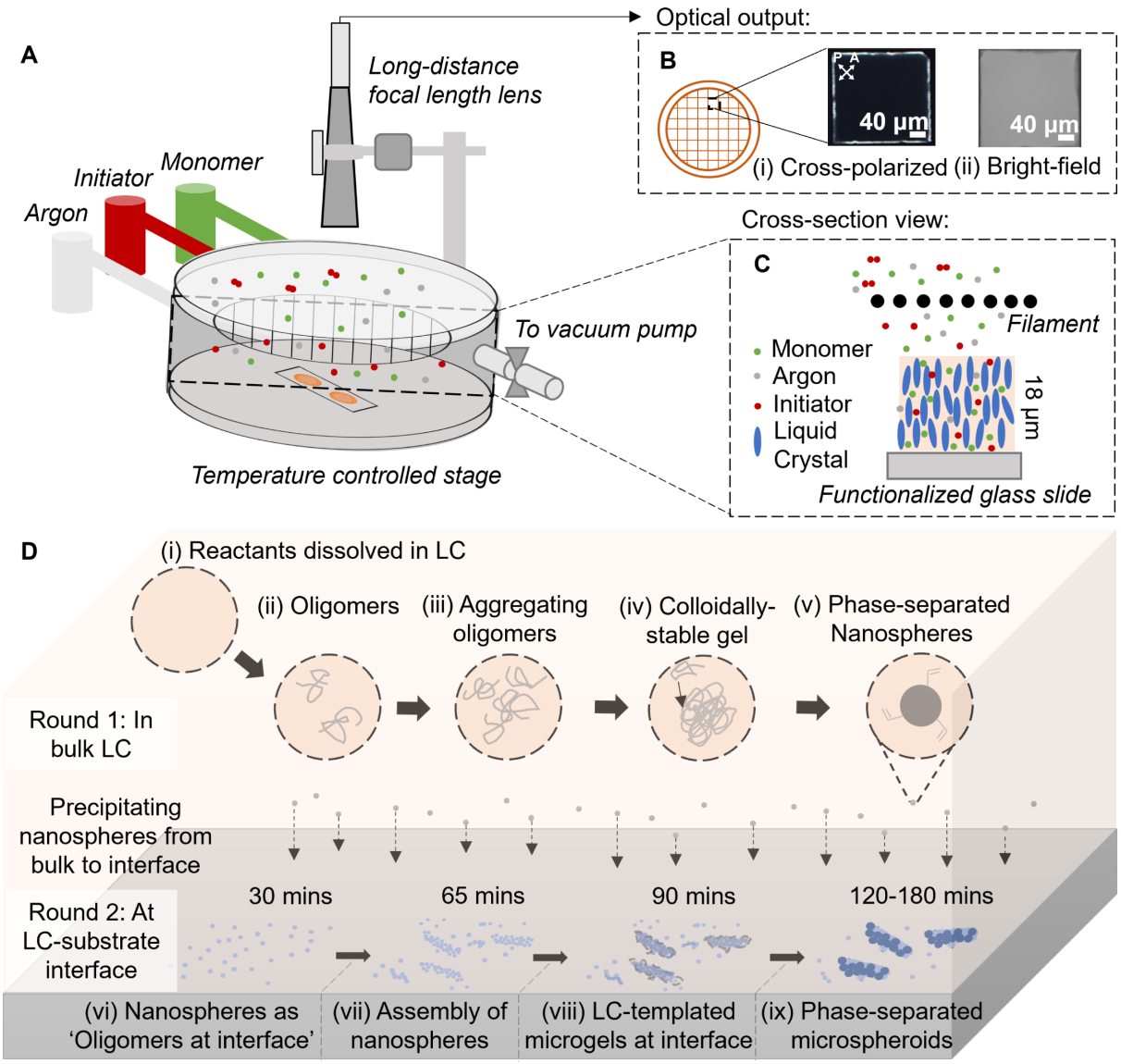

Figure 1. Overview of the iCVD-in-LC synthesis process. (A) Schema of the iCVD synthesis apparatus, (B) two examples of the optical output monitored in real time using the custom in-situ long-focal range microscope and, (C) cross-section schema of the iCVD reactor chamber, where initiator breaks down to form free radicals. The free radicals enter the LC and start polymerization upon reacting with dissolved monomers, giving rise to the polymeric particles with varying shapes. **(D) Mechanistic insights into the iCVD in LC process.** Bulk nematic LC acts as a marginal solvent, resulting in the continuous partition of pDVB nanospheres to the LC-substrate interface. The nanospheres form via the 5-step precipitation polymerization mechanism: (i) dissolution of monomer in the LC, (ii) formation

of oligomers, (iii) particle nucleation via coagulation of oligomers, (iv) growth into colloidally stable seed and, (v) phase-separation into nanosphere. The LC-substrate interface facilitates a second round of the 5-step growth, where the precipitated nanospheres at the interface (analogous to the oligomeric building blocks in bulk) form particle nuclei, LC-directed microgel clusters, and then phase-separated micron-sized shaped particles.

RESULTS

Real-time monitoring of iCVD polymerization in LC

A fundamental limitation of LC-templated polymerization has been the disruption of the LC template structure by loading monomers into the LC at a concentration sufficient to sustain the polymerization (*38*, *49*). To minimize perturbation of the LC phase by monomer dissolution, we chose iCVD based on its continuous and precise vapor-phase delivery of monomers. Furthermore, iCVD is compatible with a large library of functional monomers, enabling access to a wide palette of polymers with diverse chemical functionalities. While iCVD is presently known for its conformal coating ability over solid substrates, Gupta et al (*50*) have used iCVD in isotropic solvents such as ionic liquids and silicone oil to form 3D polymeric structures. For insoluble monomers like 1H,1H,2H,2H-perfluorodecyl acrylate (PFDA), polymerization occurred predominantly at the vapor-liquid interface, while soluble monomers such as 2-hydroxyethyl methacrylate (HEMA) infiltrate the bulk liquid, giving rise to a polymeric gel (*51*).

During iCVD in LC (Figure 1A), the monomer DVB and initiator *tert*-butyl peroxide (TBPO) are vaporized and delivered at controlled rates into the reactor under medium vacuum (150 mTorr, see Supporting Information Table S1 for detailed deposition conditions). TBPO is thermally decomposed to form *tert*-butoxide (TBO) radicals, with the energy supplied by a

filament array that is resistively heated to ~270ºC. The array is suspended over a cooled stage (kept at 20ºC, chosen to minimize evaporation of LC under vacuum, optimized for maintaining a stable LC thin film throughout the process), on which the nematic LC, E7, is placed. E7 is a commercially available LC with a broad nematic temperature range (i.e., -62 to +61ºC) (*52*), which enabled the use of a wide range of iCVD polymerization conditions. The DVB vapor and TBO radicals partition into the LC, which subsequently react to initiate polymerization via the chain-growth mechanism. To ensure that the dissolution of DVB and TBO, and the polymerization of DVB did not disrupt the alignment of the LC medium, we leveraged our custom long focal range microscope to observe the real-time progression of these processes (**Figure 2**).

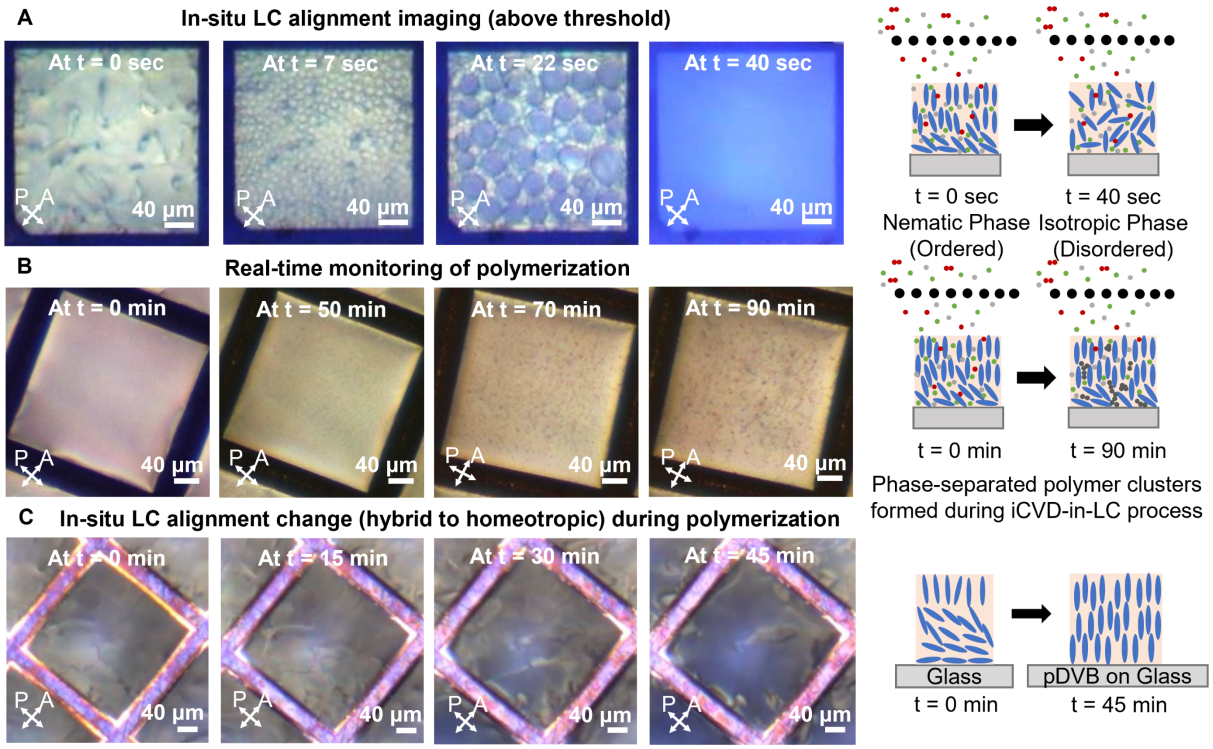

Figure 2. In-situ characterization during iCVD in LC enabled by our custom long focal range microscope. (**A**) Determination of monomer threshold concentration by observing LC phase transition from nematic (on glass with degenerate LC orientation) to isotropic phase. (**B**) In-situ observation of emergence of phase-separated polymer structures during iCVD

polymerization in LC (on glass coated by PI and then rubbed to induce uniform azimuthal orientation of LC). (**C**) Real-time monitoring of LC alignment captures the lowering of LC anchoring energy during iCVD polymerization (on glass with degenerate LC orientation).

We first identified the upper bound of DVB concentration in the LC template, above which the nematic E7 transitioned to an isotropic phase at room temperature with no long-range orientational order, as demonstrated from a series of snapshots taken in situ (Figure 2A and Supporting Information, Movie S1). The orientational order of LC was determined using cross-polarizers in the in-situ microscope. The bright appearance at t = 0 indicated the hybrid orientation of LC that is typically observed over a glass substrate (Figure 2A schematic on the left) (*53*), whereas the blue color (t = 40 seconds) indicates an isotropic liquid (Figure 2A schematic on the right; the blue color was due to light scattering from the bottom of the reactor when viewed using crossed polars). As such, we identified the threshold DVB concentration, expressed as the DVB partial pressure in the vapor phase directly above the LC, i.e., P_{DVB}, to be 30.5 mTorr (see Supporting Information Table S2 for details). The nematic to isotropic transition was signified by the formation of isotropic droplets that we observed to commonly accompany the phase transition. The P_{DVB} of 26.9 mTorr was used for all subsequent experiments. This partial pressure was used to ensure that LC stays in the nematic phase to provide the templating effect while achieving a high rate of polymerization. For the initiating species, i.e., TBPO and TBO radicals, no such transition was observed for P_{TBPO} values up to 90 mTorr. P_{TBPO} of 3.8 mTorr was used throughout this study.

iCVD polymerization was performed in the nematic LC by co-flowing DVB and TBPO (see Supporting Information Table S1 for detailed flow rates, temperatures, and pressure during iCVD). Fifty minutes after the start of the reaction (by turning on the filament array to decompose TBPO into radicals), we observed the formation of phase-separated polymeric clusters (dark dots in Figure 2B and Supporting Information, Movie S2) in LC (the beige

background). We later confirmed that these dark dots correspond to polymeric clusters using ex-situ microscopy images and SEM, as described in the next section.

The real-time monitoring also revealed a surprising effect of the polymerization, i.e., a transition of the LC alignment (on glass) from hybrid (bright appearance) to homeotropic (dark appearance) over the course of 45 minutes of DVB polymerization (Figure 2C and Supporting Information, Movie S3). We confirmed the transition by characterizing LC films obtained before (hybrid) and after (homeotropic) 65 minutes of iCVD using ex-situ orthoscopic and conoscopic polarized light microscopy (see Supporting Information, Figure S1). To unravel the origin of the transition, we prepared an optical cell with two glass slides coated using the LC-templated iCVD process, capping the top and bottom of an E7 film (see Supporting Information, Figure S1C). We argue that if the orientational transition had occurred via reorientation of the easy axis (preferred orientation) of the LC at the confining surfaces (e.g., due to polymeric structure at a surface), then the LC would maintain its perpendicular alignment in the optical cell (with dark appearance under cross-polarized light). However, the optical cell showed a bright texture (Figure S1F) corresponding to a planar alignment (Figure S1I). Therefore, we attributed the transition in Figure 2C to a low LC surface anchoring energy generated by the iCVD polymerization at the LC-substrate interface, such that the anchoring energy at the air-LC interface dictates the homeotropic alignment of the entire LC film, as shown in Figure 2C. This guided our investigation into the LC-substrate interface and our discovery of the role it plays in the LC-templated particle synthesis pathway.

Discovery of particle synthesis pathway

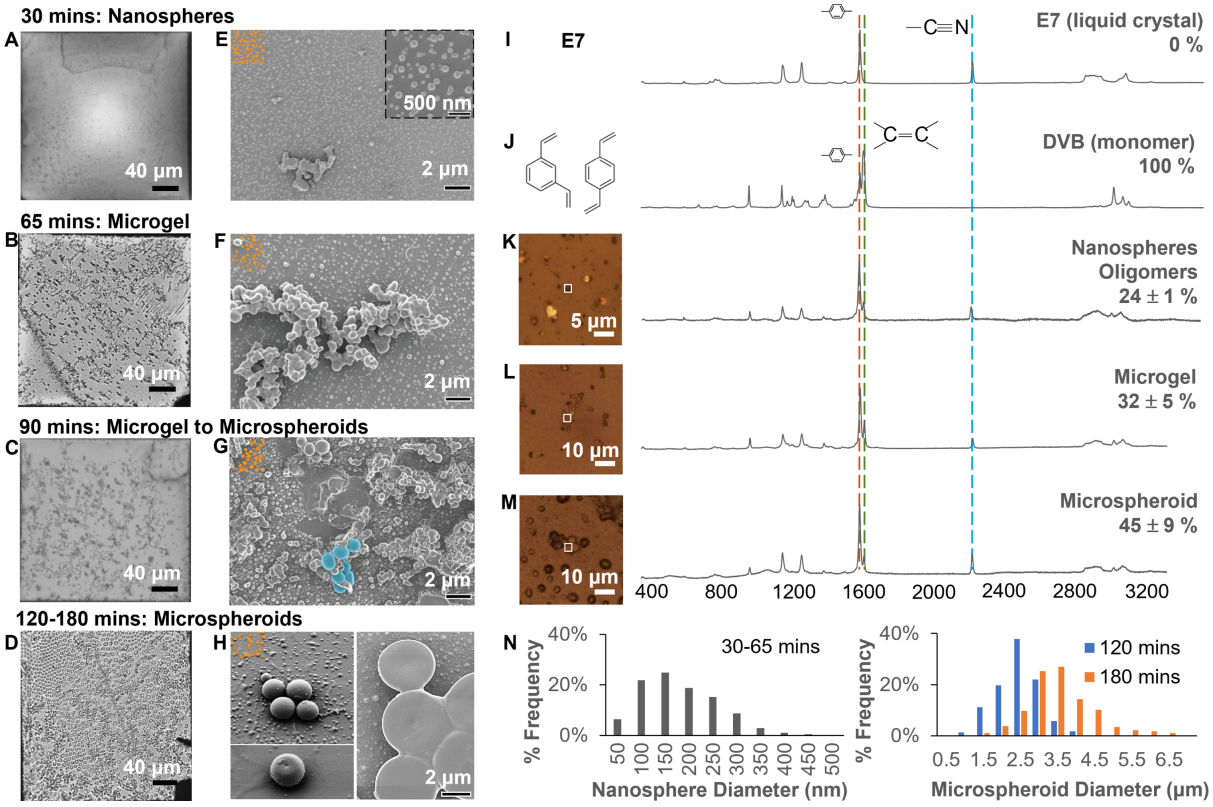

Figure 3. Progression of the morphology of pDVB particles from nanospheres to microgel clusters to microspheroids during iCVD in LC. Polyimide (PI)-coated glass was used as the substrate. **(A-D)** Ex-situ bright field optical micrographs showing the formation of shaped polymer structures (dark clusters) in LC. **(E-H)** Representative SEM images revealing the detailed shapes of the polymer particles formed at the LC-substrate interface. A subpopulation of the precipitated nanospheres is highlighted in orange (false-colored) in each SEM image to illustrate their continuous precipitation. A small number of microspheroids emerging from a microgel cluster are highlighted in blue (false-colored) in G to illustrate the microgel cluster phase separating into discrete particles. **(I-M) Laser confocal Raman microscopy of E7, DVB monomer, and the various polymer morphologies.** Microscopy images on the left in each panel show the polymer structure on which the spectrum to the right was taken; the white box indicates the excitation area. The peaks at 1609 cm^{-1} (indicated by an orange dashed line) and 2230 cm^{-1} (indicated by a blue dashed line) in the E7 spectrum correspond to the skeletal stretch of phenyl rings and CN stretch, respectively. DVB monomer also has a peak at 1609

cm^{-1} due to its benzene ring; the peak at 1632 cm^{-1} (indicated by a green dashed line) corresponds to unreacted vinyl group (i.e., C=C stretch). The percentage labeling represents unreacted vinyl bonds normalized by the total vinyl bonds in the DVB monomer, as derived from each Raman spectrum. **(N) Particle size distribution** of the nanospheres and microspheroids formed by the iCVD in LC process.

To characterize the synthesis pathway leading to polymeric particles, we stopped the iCVD polymerization in LC (on glass coated by polyimide (PI)) at predetermined times (i.e., 30, 65, 90, 120, and 180 minutes). The polymeric structures formed in LC that were first captured by in-situ monitoring (Figure 2B) were characterized further via ex-situ optical micrographs, DLS, laser confocal Raman microscopy, and SEM (Figure 3). We first used ex-situ optical microscopy to obtain high-resolution images of the LC medium containing the synthesized polymer shapes after iCVD. Subsequently, the LC film was removed by an ethanol rinse to enable the separate analyses of the bulk LC and the LC-substrate interface. The rinsing solution was collected and analyzed using DLS (Supporting Information, Figure S5). The polymer structures formed at the LC-substrate interface were dried and analyzed for their chemical compositions using laser confocal Raman microscopy and for their detailed structure using SEM. We confirmed, using Critical Point Drying (CPD), that the ethanol rinsing did not change the polymer morphology (see Supporting Information, Figure S3). A detailed description of each characterization step can be found in Materials and Methods.

Inspection of the optical micrographs (**Figure 3**A-D and Supporting Information, Figure S2 and Movie S4) and SEM of the polymeric products formed at the LC-substrate interface (Figures 3E-H) reveals a progression from nanospheres (30 mins; Figure 3A) to microgel clusters that formed from assemblies of nanospheres (65 – 90 mins; Figure 3B-C) to ultimately microspheroids (120-180 mins; Figure 3D) during DVB polymerization in LC. The SEM images provide additional detail regarding the progression of morphologies observed (Figure

3E-H). The polymeric particles formed initially (Figure 3E) are largely spherical in shape with diameters of 160 ± 80 nm (Figure 3N). Similar sizes of nanospheres are measured in bulk LC by DLS (Supporting Information, Figure S5). The nanospheres assemble to form microgel clusters (Figure 3F-G) that have a fractal-like organization and grow in size to 6.6 ± 6.4 μm effective diameter. The microspheroids that form at long times are, in contrast to the microgel clusters, compact and belong to a family of particle shapes characteristic of liquid-like behavior (microspheres, hemispherical caps etc.; Figure 3H). The Raman spectra obtained at each step along the shape-progression pathway (Figure 3K-M) contained peaks corresponding to both E7 and pDVB, suggesting that LC is encapsulated within polymer structures throughout the synthesis.

Elucidation of the particle synthesis mechanisms

By integrating the above approaches, below we unravel the key physical processes that underlie the LC-templated particle synthesis pathway. We organize our description of the pathway into three steps: (*i*) formation of nanospheres in bulk LC; (*ii*) assembly of nanospheres into microgels at the LC-solid interface; and (*iii*) emergence of microspheroids.

Our identification of these three key steps and the role that LC anisotropy played in them was aided by performing iCVD in E7 films supported by three types of solid substrates: glass functionalized by octadecyl trichlorosilane (OTS), glass, and glass functionalized with PI rubbed in one direction. E7 aligns perpendicularly at the air-LC interface. OTS-functionalized glass is known to lead to perpendicular anchoring [as shown in bottom-left (x-z plane) and bottom-right (x-y plane) panels in **Figure 4**A], which was confirmed by the dark cross-polarized optical micrograph (Figure 4A top). The glass surface (cleaned with alconox and ethanol prior to use) leads to planar anchoring with random azimuthal orientation and a hybrid orientation in the cross-section (Figure 4B). Rubbed PI-functionalized glass leads to planar

anchoring with uniform azimuthal orientation of E7 along the direction of rubbing, which was also confirmed using cross-polarized optical imaging (Figure 4C) (*53*).

(i) Formation of nanospheres in bulk LC:

The reaction mixture is initially a single phase, as evidenced by our in-situ observations revealing the absence of liquid-liquid phase boundary development during the continuous delivery of DVB into E7 (Supporting Information, Movie S4). Polymerization is initiated via the delivery of TBO radicals. Nanospheres are the dominant shape observed at the LC-substrate interface during the early stage iCVD in LC polymerization (i.e., first 30 mins, Figure 3E). We believe the nanospheres formed in bulk LC and continuously partition to the LC-substrate interface as they are captured at the LC-substrate interface throughout the polymerization (Figure 3E-H, with a subpopulation of the nanospheres highlighted in orange). DLS performed on the bulk LC (collected via the aforementioned rinsing step) confirmed the presence of nanospheres of similar sizes (Supporting Information, Figure S5).

We attributed the formation of nanospheres to the phase separation of pDVB from the marginal solvent (i.e., E7), building upon the mechanism of precipitation polymerization of DVB in isotropic solvents.(*32*) The nanospheres have 24 ± 1 % unreacted vinyl groups (Figure 3K), which is common for precipitation polymerization (*54*). However, the percentage is lower than that for pDVB synthesized via conventional iCVD (i.e., 52%) (*55*), which is likely a result of the low threshold concentration of DVB in nematic LC and, hence, the diffusion-limited reaction conditions.

The nanospheres have an average diameter of 160 ± 80 nm (Figure 3N), calculated using a sample size of 15417 particles at the LC-substrate interface (see Supporting Information for methodology). That size distribution was corroborated by DLS performed on bulk LC (Supporting Information, Figure S5). This average size is an order of magnitude smaller than

that obtained in common precipitation polymerization, i.e., 2-5 μm (*32*, *56–58*), which we attribute to the combined effects of (i) the marginal solvency of pDVB in nematic E7, and (ii) the poor dispersion of nanospheres that are larger than the extrapolation length of E7 (~100 nm) (*39*), owing to the elastic energy that arises from LC director strain (*59*). Here we note that the extrapolation length of LC is defined as the ratio of a characteristic Frank elastic constant to the LC-surface anchoring energy density, which has also been postulated to determine the diameters of nanofibers synthesized in LC (see Supporting Information for a detailed discussion on the interactions between an introduced particle and a nematic LC host) (*39*). This conclusion is supported by the prior observation that nanospheres with similar sizes (300 ± 100 nm) have been obtained by polymerization of crosslinkers in LC (*41*, *60*). This stage of iCVD polymerization undergoes a similar growth pathway in LC that is supported by OTS-functionalized glass, glass, and PI-functionalized glass (with the latter described in detail above; see Supporting Information Figures S6-9 for discussions on polymer morphology progression during iCVD in LC on the other two surfaces).

To understand this step, we calculated the magnitudes of the key contributions to the free energies that characterize the dispersions of nanospheres in LCs. In this calculation, we describe the elastic properties of E7 by a single Frank elastic constant of $\kappa = 14.4$ pN (*39*). By taking the surface tension of E7 (*61*) as 24.2 mN/m and the surface tension of pDVB (*62*) as 42 mN/m, we estimate the interfacial tension between pDVB and E7 as:

$$\Upsilon_{pDVB\text{-}E7} = \Upsilon_{pDVB} - \Upsilon_{E7}\cos\theta = 17.9 \text{ mN/m}$$

where θ is the contact angle of E7 on pDVB surface. We measured the contact angle of E7 on a silicon wafer surface coated with pDVB thin film by iCVD to be less than 5º.

The nanospheres diameter was measured as 160 ± 80 nm, which is greater than the LC extrapolation length (typically ~ 100 nm) (*39*). Hence, we calculate the elastic energy associated with the straining of LC around the nanoparticle to be :

$$\kappa r = 14.4 \times 10^{-12} \times 80 \times 10^{-9} = 1.2 \times 10^{-18} J$$

The corresponding interfacial energy is:

$$4\pi r^2 \Upsilon_{pDVB-E7} = 4 \times \pi \times (80 \times 10^{-9})^2 \times 17.9 \times 10^{-3} = 1.4 \times 10^{-15} J$$

These calculations reveal that the interfacial energy is over three orders of magnitude greater than the elastic energy, consistent with our observation that the nanoparticles are largely spherical (Figure 3E). We note, however, that interfacial tensions between LC and isotropic oil phases that are one to three orders of magnitude smaller than our estimate of 18 mN/m are not uncommon (*63*), suggesting that access to non-spherical nanoparticles may be achieved in future studies by appropriate interfacial engineering. In the current study, however, a spherical nanoparticle shape is the starting shape obtained in the synthesis pathway for polymerization in LC (with the three molecular alignments). Intriguingly, as these nanospheres assemble at the LC-solid interface, they are organized by elastic forces of the LC into elongated microgels.

(ii) Assembly of nanospheres into microgels at the LC-solid interface:

In contrast to precipitation polymerization, during which pDVB seed particles form mainly during early-stage polymerization, nanospheres continue to form and partition to the LC-substrate interface throughout the iCVD process in the LC (e.g., on top and around the polymeric structures that later formed, with a subpopulation false-colored in orange in the upper left corners of Figure 3E-H). This observation highlights a key difference between the batch-wise reaction in precipitation polymerization, where solutions were preloaded with a

finite amount of initiator and monomer, and the continuous reaction we performed with constant delivery of DVB and TBPO into nematic E7 throughout the reaction time.

We observed that the partitioned nanospheres assemble at the LC-substrate interface, forming colloidally stable microgels after 65 minutes of iCVD polymerization (Figure 3F). With the continuous partition of the nanospheres, microgels grow by capturing the nanospheres. In addition, heterogeneous polymerization occurs at the microgel-LC interface, leading to further microgel growth, which is supported by Raman microscopy (Figure 3L). These microgel clusters have 32 ± 5 % unreacted vinyl groups, which is higher than the partitioned nanospheres and consistent with heterogeneous polymerization.

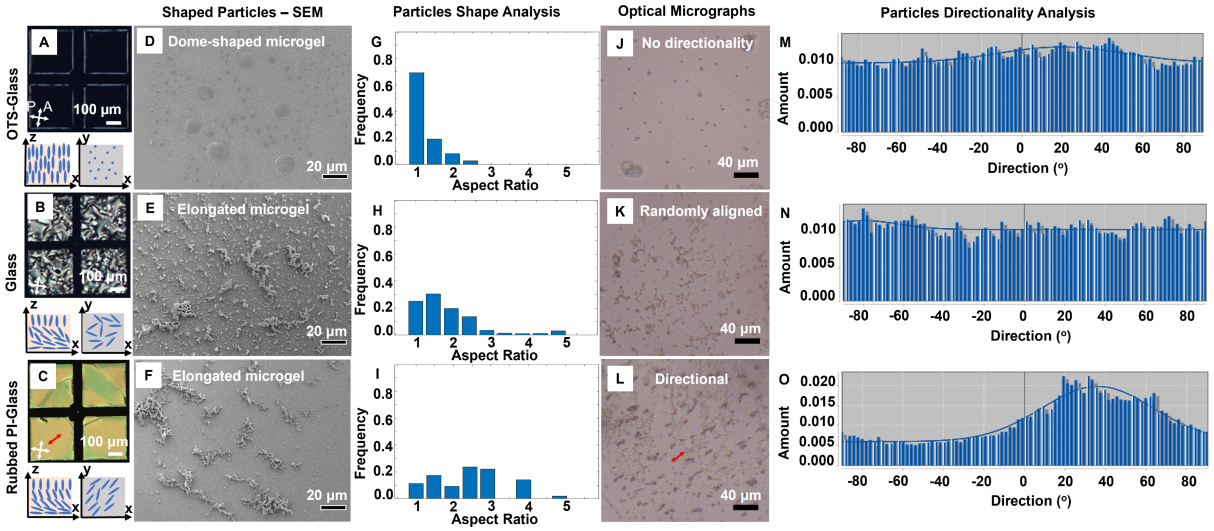

Figure 4. Role of LC alignment in shaping and directing microgel clusters. (**A-C)** LC alignment on the three solid substrates used in this work: glass functionalized by OTS, bare glass, and glass coated by PI and then rubbed. In each panel, the representative cross-polarized micrographs are accompanied by the corresponding schematics showing the orientation of E7 in the x-z plane (i.e., cross-section) and x-y plane (i.e., top-down at the LC-substrate interface), respectively. The red arrow corresponds to the rubbing direction on the PI substrate. (**D-F)** SEM images of the polymeric structures formed in each LC template: OTS-treated glass, bare

glass, and glass covered by rubbed PI led to dome-shaped, randomly oriented, and directional microgel clusters, respectively. (**G-I)** The frequency of appearance of microgel clusters with specific aspect ratios, revealing the statistics of shape anisotropy on the three substrates. OTS-treated glass led to circular or near-circular shape due to the homeotropic alignment of E7; bare glass and glass covered by rubbed PI led to elongated microgels due to their hybrid alignment of E7, as shown in the x-z plane orientation in A-C. (**J-L)** Bright field optical micrographs obtained for the three substrates, where polymeric clusters appear dark. The red arrow corresponds to the rubbing direction of the PI substrate. (**M-O**) Directionality analysis of the polymeric clusters in J-L, highlighting the aligned polymeric structures on rubbed PI (O), oriented along the presumed direction of rubbing, in contrast to the absence of directionality on OTS-treated glass and bare glass (M, N).

While precipitation polymerization often leads to spherical microgels,(*32*) the shapes of microgels observed in Figure 3F are guided by the local orientation of the LC. The SEM images of the microgels formed on the three substrates (Figure 4D-F) clearly indicate the directed growth of disparate polymer morphologies. That apparent shape anisotropy is quantitatively demonstrated through a statistical analysis of the frequency of appearance of the microgel clusters with distinct aspect ratios on each substrate (detailed methodology is described in Materials and Methods section). We observed dome-shaped microgels (aspect ratio = 1) to emerge on OTS-functionalized glass (Figure 4D, 4G) with homeotropic E7 alignment. In contrast, elongated particles with higher aspect ratios dominate in E7 with hybrid alignment, i.e., on glass and rubbed PI-functionalized glass. Specifically, unmodified glass leads to randomly aligned microgels (Figure 4E, 4H), whereas directional microgels (oriented along the presumed direction of rubbing) form on a rubbed PI surface (Figure 4F, 4I).

Based on these microscopic observations, we performed large-scale particle directionality analysis at the length scale of a few millimeters on polymer microgels observed in optical micrographs (Figure 4J-L, the detailed methodology is described in Supporting Information). The directionality histograms show that the microgels formed on OTS-functionalized glass and glass are randomly aligned (Figure 4M, 4N), and those formed on rubbed PI are aligned at an angle of 36 ± 1 º (Figure 4O), i.e., the direction of rubbing. This directionality is further seen through the continuous alignment of microgels over the length scale of an entire TEM grid (e.g., 3.05 mm across; see Supporting Information, Figure S10). The disparate shapes and directionality of microgel clusters on the three substrates are obtained due to the anisotropic diffusion of nanospheres on the substrate during kinetic aggregation, driven by the local orientation of LC molecules. Also, note that the shape progression is observed to be slower on OTS-functionalized substrate, with the growth of microgels continuing for 180 minutes (Figure S7G-J), in comparison to microgel growth on glass over 90 minutes (Figure S6G) and PI-functionalized substrate (Figure 3G) owing to out of plane orientation of LC molecules.

(iii) Emergence of microspheroids at the LC-solid interface:

On continuing the polymerization for a longer time (90 minutes), we observe the emergence of microparticles from these microgel clusters (Figure 3G). Specifically, iCVD polymerization in LC for 120 minutes led to the formation of microspheroids, a family of polymer particles whose shapes resemble liquid drops (Figure 3H on PI-functionalized glass and Figure S6G on glass). Further polymerization for 180 minutes allowed the microspheroids to grow from 2.2 ± 0.6 μm to 3.3 ± 0.9 μm in diameter (Figure 3N and Figure S9G). These microspheroidal particles were found to induce weak tangential anchoring of the LC. This was confirmed by collecting these particles post synthesis and dispersing them in an LC filled optical cell with

homogeneous planar anchoring on the confining surfaces. The absence of any optical signatures resembling a topological defect under brightfield imaging (Figure S11C) and the presence of four optical lobes surrounding the particles when viewed under crossed polarizers (Figure S11D) provide support for our conclusions regarding weak tangential anchoring.

To understand the driving force for the shapes of the microspheroids, we compare the free energy of a linear cluster of nanospheres in LC and a spherical microspheroid composed of the same number of nanosphere building blocks. The radius of a nanosphere is taken to be 80 nm and that of a microspheroid 1 μm, based on our SEM results (Figure 3N). As such, the number of nanospheres contained in each microspheroid is estimated by equating the volume of the microspheroid to the total volume of nanosphere constituents, i.e., $R^3 = Nr^3$, which yields an estimate of N of 2000. The free energy of the N nanospheres arranged in a linear configuration is approximated as the sum of their elastic energies, surface anchoring energies, and interfacial free energies:

$$E_1 = N(\kappa r + Wr^2 + 4\pi r^2 \Upsilon_{pDVB-E7})$$

$$= 2000 \times [14.4 \times 10^{-12} \times 80 \times 10^{-9} + 6 \times 10^{-5} \times (80 \times 10^{-9})^2$$

$$+ 4\pi \times (80 \times 10^{-9})^2 \times 17.9 \times 10^{-3}]$$

$$= 2000 \times [1.2 \times 10^{-18} + 3.8 \times 10^{-19} + 1.4 \times 10^{-15}] \sim 2.9 \times 10^{-12} J$$

where $W = 6 \times 10^{-5}$ J/m^2 (*64*) which is surface anchoring energy density for 5CB on PS at 31 ^{o}C.

The free energy of the same N nanospheres arranged in a spherical configuration would give rise to the same interfacial free energy, as the total surface area remains the same irrespective of the organization of the particles. However, it is important to note that heterogeneous polymerization is also occurring at the particle-LC interface during the reconfiguration of the nanospheres, as evidenced by our Raman microscopy results, i.e.,

microgel clusters have more unreacted vinyl groups compared to nanospheres (Figure 3K vs. 3L), and there is a further increase in % unreacted vinyl group in the formed microspheroids to 45 ± 9 % (Figure 3M). It is also possible that the heterogeneous polymerization bridges nanospheres, thus promoting the formation of compact shapes that maximize the number of bridges over the LC elastic forces (analogous to particle organizations driven by capillary bonds) (*65*). Accordingly, the free energy of the N nanospheres assembled within a microspheroid with a radius of 1 μm is estimated as:

$$E_2 = \kappa R + WR^2 + 4\pi R^2 \Upsilon_{pDVB-E7}$$

$$= 14.4 \times 10^{-12} \times 1 \times 10^{-6} + 6 \times 10^{-5} \times (1 \times 10^{-6})^2 + 4\pi \times (1 \times 10^{-6})^2 \times 17.9 \times 10^{-3}$$

$$= 1.4 \times 10^{-17} + 6 \times 10^{-17} + 2.2 \times 10^{-13} \sim 2.2 \times 10^{-13} J$$

The calculation above leads us to predict that the spherical microspheroids have free energy that is one order of magnitude lower than that of linear clusters, providing a thermodynamic driving force for the reorganization of nanospheres into the observed microspheroid shapes. Moreover, the interfacial energy is over three orders of magnitude greater than the elastic energy for microspheroids with a radius of 1 μm, consistent with our observation that the microspheroids formed belong to the family of liquid-like shapes having spherical cross sections. We note also that the reorganization of the nanospheres from a linear configuration to a spherical one is possible because the nanospheres are mobile at the LC-substrate interface. As discussed below, our analysis suggests that the limiting size of the as-formed microspheroids is determined by this mobility, with each cluster giving rise to multiple microspheroids (instead of one large one).

The pathway proposed for the emergence of multiple microspheroids from a single microgel cluster and multiple nanospheres is supported by SEM images collected at 90 minutes (Figure S12 and Figure S13), which captured several mid-transition clusters. We observed that

neighboring microspheroids are often arranged in a linear chain, hinting at their origin from the same elongated microgel cluster. This observation can be understood from the small diffusion length of the nanospheres in comparison to the lateral size of the microgel cluster. The nanosphere diffusion length (order of magnitude) is estimated using diffusion coefficients predicted by the Stokes-Einstein equation:

$$D = \frac{k_B T}{6\pi\eta r} \sim 0.07\ \mu m^2/s$$

where r is the average nanosphere radius and η is the bulk viscosity of the LC (*66*), taken here as 39 mPa-s. The diffusion length is then calculated as 2.9 μm < x = $\sqrt{2Dt}$ < 9.1 μm, where t is the time taken for the microspheroids to emerge from microgel clusters (1 < t < 10 minutes). In addition, we argue that the actual diffusion coefficient, and hence the diffusion length, would be smaller than the theoretical value calculated above due to resistance added by the solid surface and heterogenous polymerization at the solid-LC interface. Thus, the actual diffusion length of nanospheres is likely to be smaller than the lateral size of the microgel clusters (ranging from 0.5 to 51.4 μm in a population), thereby forming multiple microspheroids of diameter 2-4 μm from a single microgel cluster.

The transformation of the microgel clusters into microspheroids, as described above, does not occur in the bulk of the LC, but rather, it occurs in the environment defined by the LC-substrate interface. We observed a range of polymer morphologies to emerge in the interfacial environment, depending on the LC orientation on different solid substrates and the reaction time (Figure 5A). By 65 minutes (when microgel emerges), the influence of the supporting surface was evident, with dome-shaped microgels on the surface supporting homeotropic LC and elongated microgels on surfaces supporting LC with hybrid alignments near the surface. After 120-180 minutes of iCVD, microspheroids with different shapes (spheres and hemispherical caps, with low-contact-angle caps resembling discs) were obtained in LC with

hybrid alignment. The iCVD conditions (i.e., monomer and initiator flow rates, total chamber pressure, and stage temperatures) were kept constant in these depositions (see Supporting Information, Table S1 for detailed deposition conditions). Engineering these deposition conditions will, we predict, lead to a greater morphological diversity, which will be a focus of our future studies.

When combined, our results obtained via in-situ optical microscopy, SEM, and Raman microscopy point to a strategy to achieve shaped polymer particles simply by controlling the polymerization reaction time in LC and LC alignment. Further, we mapped the polymerization pathway along a particular trajectory, which led to the discovery of a family of polymer particles whose shapes resemble liquid drops due to the dominating effects of the interfacial tensions (suggesting we can access non-equilibrium contact angles leading to the diversity of shapes). While one particular trajectory was elucidated in this paper, there are other permutations of the monomer-LC-substrate combination, particularly ones with lower interfacial energy that would enable particle shape control by leveraging the other energy terms (e.g., LC elastic energy). The mechanistic insights elucidated in this section provide a roadmap to the design and synthesis of shape-controlled particles.

In addition to particles obtained at LC-substrate interfaces, we also observed the formation of a porous film at the LC-vapor interface for longer reaction times (e.g., longer than 120 mins), as shown in Supporting Information, Figure S14. Similar observations have been made during iCVD in isotropic liquids and are likely due to monomer adsorption at the LC-vapor interface (*67*). Wei et al., in a recent study, characterized the film morphology on different liquids (including isotropic liquids and nematic LC) in detail (*68*). We refer readers to these studies to learn more about the formation of polymer thin films at the LC-vapor interface.

Synthesis capabilities and potential applications

We envisage shape-controlled particles synthesized by LC-templated iCVD to have a broad range of impact as carriers of small-molecule active ingredients in applications such as targeted drug delivery (*7*), microencapsulated pesticides (*69*), and in food industry for enhancement in flavors and fragrances (*70*). Here we briefly demonstrate their potential as drug delivery vehicles. The E7 encapsulated in the particles (as indicated by the CN peak at 2230 cm^{-1} in their Raman spectra, Figure 3K-M), can be viewed as a proxy for therapeutics. To demonstrate the ability to release similar molecules, we studied the Raman spectra for microspheroids before and after immersing in ethanol for 10 mins. Disappearance of the CN peak at 2230 cm^{-1} after release (Figure 5B) indicates successful release of the encapsulated E7 molecules with no change in the polymer composition (i.e., % unreacted vinyl bonds) (see Supporting Information, Figure S15). Although the release conditions will likely need to be modified to adapt the particles for a particular application, we believe this proof-of-principle points to their exciting future potential. For example, small-molecule therapeutics could be dissolved in E7 with a deliberate selection of polymer chemistry that promotes strong interaction with the therapeutics (e.g., via hydrogen bonding). Such incorporation of therapeutics is predicted to enhance their retention, while E7 can be easily removed via an ethanol wash. We also note the heterogeneity in particle sizes shown in Figure 5A and 5B, which can be desirable for programming the pharmacokinetics using a carefully selected collection of such particles.

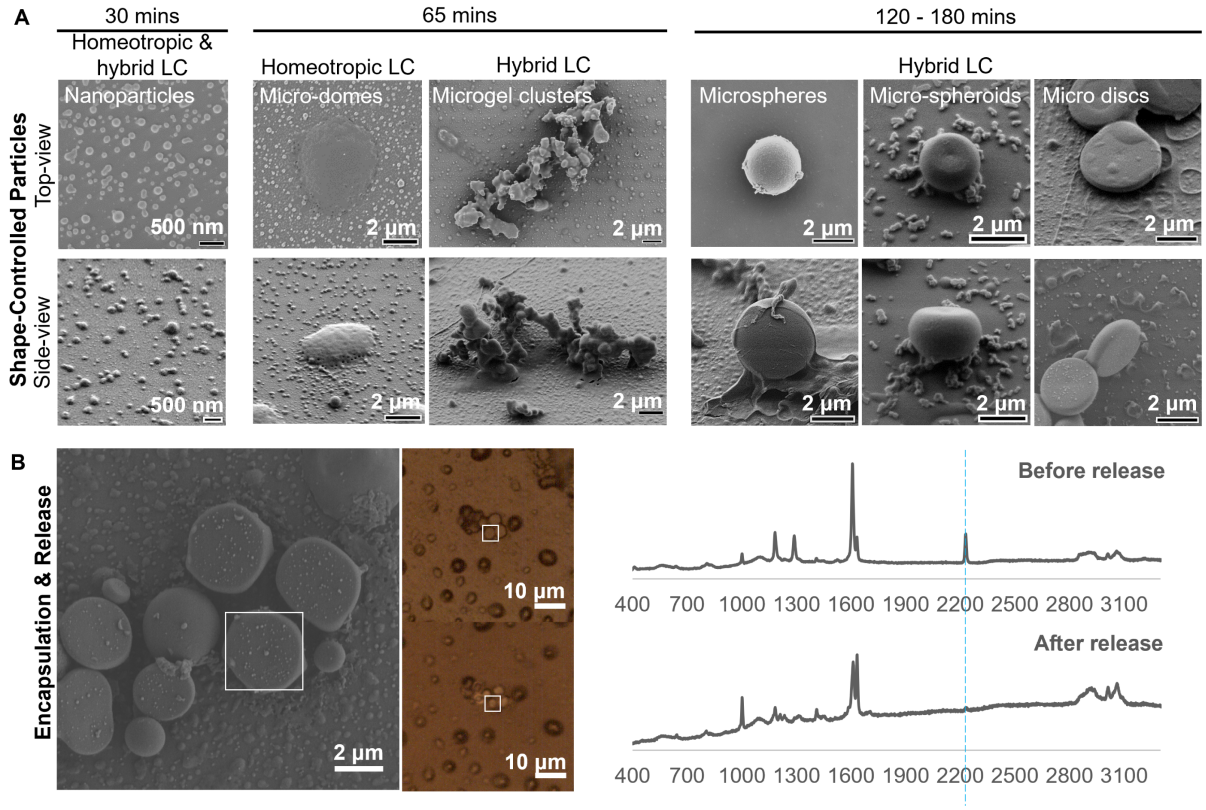

Figure 5. Synthesis capabilities of the iCVD-in-LC process. (A) Synthesis of shaped polymeric particles using iCVD in LC. SEM images of the particle shapes (top & side views) that show the detailed polymer morphology at different growth stages. Although different samples were examined in the top- versus side-view SEM images, they were synthesized under identical conditions, reaction time, and LC template. Nanoparticles are synthesized by performing iCVD for 30 minutes in both homeotropic and hybrid LCs; hemispherical domes and elongated clusters are formed by performing iCVD for 65 minutes in homeotropic and hybrid LC, respectively; microspheroids with different shapes (spheres and hemispherical caps, with low-contact angle caps resembling discs) are formed by performing iCVD between 120-180 minutes in hybrid LC. Homeotropic LC also leads to microsphere and thus not included here (see Figure S7 for details). **(B) Encapsulation and release of E7 molecules by the shape-controlled particles.** SEM image (left) of the corresponding particle for which the Raman spectra (right) were collected and, microscopy image (middle) and the Raman spectra (right) obtained before and after release of E7, respectively.

DISCUSSION

The key finding reported in this paper is the discovery of pathways governing the synthesis of polymeric structures in a supported LC film, which led to disparate morphologies, using DVB as the monomer for demonstration. Drawing inspiration from the well-understood mechanisms of DVB precipitation polymerization in isotropic solvents, we revealed that LC-templated iCVD polymerization passes along the precipitation growth pathway twice, once in bulk and the second time at the LC-substrate interface. This two-step pathway provides an effective framework for understanding the mechanism of polymerization in anisotropic solvents. It also enabled us to achieve polymer morphologies beyond spheres and films commonly observed in isotropic solvents (see Supporting Information for a detailed discussion on polymer shapes obtained for iCVD polymerization in isotropic solvents). The templating effects of LC were demonstrated using three types of LC alignments, carefully selected to have different orientations near the LC-substrate interface, which enabled us to imprint LC anisotropy on the polymeric microgels, an initial step towards shape programmability. A wide selection of LC templates, or even engineered defects in LC, could be leveraged in future research to achieve a broader palette of polymer morphology.

Those insights were enabled in part by the technical advancement of in situ and real-time monitoring of the iCVD polymerization in LC. An in-situ reflectance microscope serves as an in-line monitoring technique to obtain the targeted polymer shapes while maintaining the anisotropy of the medium. The obtainment of targeted shapes also requires meticulous tuning of the reaction conditions, which was enabled by the precision synthesis capability of iCVD, such as continuous vapor reactant delivery with precise compositions of initiator and monomer. In addition, iCVD also provides the ability to effectively decouple the initiator and monomer concentrations and types, which could lead to unprecedented particle shapes and controllable

size distributions upon further optimization. Furthermore, iCVD is compatible with a library of over 70 monomer chemistries, which can be harnessed to enable endless combinations of morphology and organic functionality using the reported synthesis approach. In one example, iCVD polymers include biocompatible materials that have been used in drug delivery and tissue engineering (*71–73*).

With the library of polymer chemistries that have been demonstrated using the iCVD technique and numerous LC chemistries and alignments available, there are many degrees of freedom to control the synthesis conditions. That versatility is a major merit of the reported synthesis approach of iCVD in LC. Nevertheless, we emphasize that the current work focuses on elucidating the pathways of particle shape formation during continuous polymerization in LC. That understanding, while obtained using a limited set of conditions, is foundational for the exploration of the many degrees of freedom in future investigations. We will focus on several crucial directions, such as understanding the effects of polymer chemistry and other LC phases (smectic, cholesteric) on shape formation and of reaction conditions such as initiator concentration on the polymerization mechanism and the resultant polymer morphology.

This work demonstrates that iCVD is a versatile tool for the synthesis, characterization, and mechanistic investigation of polymerization templated by structured liquids. Its compatibility with established manufacturing technologies, such as roll-to-roll semicontinuous deposition, makes it an attractive approach for the design and manufacturing of functional polymeric particles with targeted shapes. Although additional studies are needed to define the production throughput of the technology at this stage, there are many degrees of freedom to explore and optimize in order to fully realize its manufacturing potential, such as alternative reactor designs to incorporate state-of-the-art imaging modalities. That capability will benefit many existing and future technologies, ranging from shape-programmed pharmacokinetics in drug delivery to shape-controlled motion and group behavior in fluids for soft robotics.

MATERIALS AND METHODS

Materials

We obtained the nematic LC, E7 (nematic mixture of cyanobiphenyls and terphenyls), from EMD Millipore (Billerica, MA). Divinylbenzene (technical grade, 80%), hexane (CHROMA SOLV ® grade), and octyltrichlorosilane (OTS) were purchased from Sigma-Aldrich (St. Louis, MO) and used as received. Polyimide and thinner solutions were purchased from HD MicroSystems (Parlin, NJ). Ethanol (anhydrous, 200 proof) was purchased from VWR International (Radnor, PA) and used as received. TEM copper grids and quartz slides were purchased from Electron Microscopy Sciences (Hatfield, PA).

LC templates preparation

Substrate Preparation: Glass substrates were prepared by incubating a glass slide in alconox solution and sonicating for 10 minutes, followed by a thorough rinse in deionized water (DI-H_2O) and ethanol. To functionalize glass substrates with OTS, they were first incubated in a hexane solution of OTS (324uL in 140mL hexane) for 30 minutes, followed by rinsing with chloroform for 1 min and were then thoroughly rinsed in deionized water (DI-H_2O) and ethanol. To functionalize glass substrates with PI, polyimide (PE2555) and thinner solutions were mixed (1:1 wt/wt) in a vial and vortexed for 30 seconds. The mixture was filtered with a 0.45-μm pore size filter. Glass substrates (rinsed with ethanol) were then spin-coated with the filtered PI + thinner mixture (3000RPM for 25 seconds). This was followed by baking the surfaces at 275ºC for 1 hr and then rubbing them unidirectionally with a velvet cloth.

Preparation of LC Templates: We have used a copper TEM grid containing slots, each with a dimension of 285 μm x 285 μm, to create flat LC films. On performing the polymerization in LC-filled TEM grids with different compositions (copper or molybdenum coatings) or dimensions (285 μm x 285 μm or 95 μm x 95 μm), no change was observed from the optical

micrographs capturing the polymer structures formed and LC alignment after 65 minutes of polymerization on OTS functionalized substrate as seen in Figure S16.

Characterization Methodologies

Microscopy: An Olympus BX41 microscope with 4X and 20X objectives, two rotating polarizers, and a Moticam 10.0 MP camera was used for optical microscopy. In addition to crossed polarizers in the above microscope setup, a Bertrand lens was used for conoscopic polarized light microscopy. For in-situ microscopy, a custom setup with Keyence VHX 970F long-focal length (85mm) microscope lens (50x to 500x magnification) was installed directly over iCVD reactor chamber using a boom arm assembly. This custom assembly captured real-time videos of the polymerization process in bright-field mode (e.g., Movie S4), and real-time dynamic LC molecular alignment (e.g., Movie S3) by adding two crossed polarizers in the path of light (a stationary polarizer before the light reaches the sample and a rotating polarizer after the light is reflected from the sample). Owing to the storage limitation of the microscope, we can record a video continuously for 60 minutes. To monitor the process further, such as in Movie S2, we start another recording, which requires handling the microscope that could potentially shift its position slightly and result in mismatches of frames. As a precaution, while capturing multiple videos to monitor longer reactions, we keep the focus on the same grids throughout the process, as highlighted in Figure S17. Scanning electron microscopy (SEM) images were captured at an acceleration voltage of 2 kV on samples that had been coated with approximately 3 nm of gold/ palladium using a Zeiss LEO 1550 field emission scanning electron microscope (FESEM).

Dynamic Light Scattering (DLS): Ethanol solutions (1 mL each) of the polymers prepared by iCVD-in-LC were placed in glass tubes and sonicated for 30 minutes. Dynamic light scattering measurements (Brookhaven Instrument) at room temperature were recorded at light scattering

angles of 90° using a laser of wavelength 638 nm, and the corresponding autocorrelation functions were generated. The autocorrelation functions were analyzed using the CONTIN algorithm to calculate the hydrodynamic diameters of the polymer particles in the ethanol solution.

Critical Point Drying (CPD): Since solvent evaporation induces capillary forces that can affect the shape of the particles, we employed a CPD procedure to scrutinize the effect of the solvents used during the post-processing washing step (e.g., ethanol, isopropanol) on the particle shape. In this method, the iCVD-in-LC polymerized samples were immersed in a bath of isopropanol, which was then replaced with liquid carbon dioxide using a LEICA CPD300. The isopropanol substitution by liquid CO_2 was performed for 12 cycles. The CO_2 was then removed at the critical temperature (31°C and 74 bar) to avoid the generation of a meniscus and capillary forces acting on the polymer network owing to the similar density of the liquid and its vapor.

Raman microscopy: Raman spectra were collected on samples prior to SEM using Renishaw InVia Confocal Raman imaging microscope. All spectra were recorded using excitation with a 532 nm laser at 40mW with a spatial resolution of ~ 1μm and spectral resolution of ~ 1 cm^{-1} using 2400 lines/mm grating and an edge filter with a CCD camera detector. Two objectives were used: 50x (N.A. 0.45 for Raman imaging, long-working distance with estimated axial resolution ~ 2.6 μm) and 100x (N.A. 0.9 for Raman imaging with estimated axial resolution ~ 0.7 μm).

Table 1: Spectral acquisition conditions used were as follows:

Sample type	**Raman shift (cm^{-1})**	**Exposure time (sec)**	**Laser power (%)**	**Shutter (%)**	**Number of Scans**
DVB	400 – 3600	10	10	10	3
E7	400 – 3600	10	50	50	3

Qualitative analysis spectra for particles	300 - 3300	10	50	50	3
Quantitative analysis spectra for particles	1340 - 2400	10	50	50	10

For qualitative composition analysis, conditions were optimized (Table 1) to capture the entire spectral range to identify all peaks for individual particles, E7 and DVB, without detector saturation. To capture individual nanoparticles, 100x objective was used, while 50x (long-working distance) was used to capture individual micron-sized particles. However, to capture all the data used for quantitative comparisons, a 50x (long-working distance) objective was used, with the same spectral acquisition parameters as mentioned above. This was to ensure the same spatial resolution (both lateral and axial) to capture the evolution of chemical compositions of particles synthesized throughout the shape progression in iCVD-in-LC polymerization at the LC-substrate interface.

Raman Spectra Peak Analysis and Calculation of % Unreacted Vinyl Bonds

Signature Peaks: As benchmarks, we first obtained the Raman spectra for nematic E7 (Figure 3I; see Supporting Information, Figure S4 for the molecular structure of constituents for the E7 LC mixture) and DVB monomer (Figure 3J) used, which agreed well with literature (*74–78*). Briefly, peaks at 1184 and 1609 cm^{-1} correspond to aromatic CH in-plane deformation and C=C skeletal stretch of phenyl rings of E7, respectively. The peaks in the region of 2850-2950 cm^{-1} are from the aliphatic chains attached to the benzene ring in E7, and peaks 3010-3100 cm^{-1} are due to the CH stretch of the benzene ring. The peak at 1288 cm^{-1} is due to the C-C stretch of the biphenyl bond, and the peak at 2230 cm^{-1} is due to the CN stretch, which is the signature peak used here since it is proportional to a number of E7 molecules, and it occupies a region

without any overlap with the DVB peaks (*74–76*). Prominent peaks for DVB monomer correspond to breathing vibrational mode and skeletal stretch of benzene ring at 1000 and 1609 cm^{-1}, respectively. The peaks in the range of 1150-1200 cm^{-1} correspond to C-C stretches, and in the range of 3000-3100 cm^{-1} belong to C-H stretches. The peak at 1632 cm^{-1} corresponds to the C=C stretch of the unreacted vinyl group, which is of importance to us in calculating the percentage of the unreacted vinyl bonds in pDVB (*77*, *78*). This is also the signature peak of DVB that does not overlap with peaks of E7. In summary, the three peaks used to estimate unreacted vinyl bonds of polymer particles include the nitrile peak (2230 cm^{-1}) in E7, C=C stretching of unreacted vinyl bonds in DVB (1632 cm^{-1}), and ring skeletal stretch shared by E7 and DVB (1609 cm^{-1}).

Quantitative Analysis: To quantify the % of unreacted vinyl groups, we deconvoluted the peaks at 1583, 1609, and 1632 cm^{-1} and calculated the peak areas for the three peaks of importance at 1609, 1632, and 2230 cm^{-1} using Origin data analysis software (OriginLab, MA). For that calculation, we first plotted the spectra from obtained data, followed by software-guided peak analysis, which included background subtraction (using an interpolated user-defined baseline by identifying 8-10 anchor points on the baseline of spectra), peak deconvolution, and area integration. Next, using the ratio of peak areas corresponding to the phenyl ring (at 1609 cm^{-1}) and CN stretch (at 2230 cm^{-1}) obtained for E7 as a reference, we deconvoluted the contribution to peak area (of 1609 cm^{-1}) of phenyl rings in E7 and pDVB for all polymeric structures. Taking the ring to unreacted vinyl peak area ratio in DVB spectra as reference, we then calculated the percentage of vinyl groups left unreacted in each particle using the ratio of the peak areas corresponding to rings of pDVB (deconvoluted in the previous step from peak at 1609 cm^{-1}) to unreacted vinyl (at 1632 cm^{-1}).

Image Processing and Statistical Analysis

False coloring in Figure 3E-H was done using Adobe Illustrator by manually defining particle boundaries and overlaying a colored mask on top of the nanoparticles (orange) and microparticles (blue) present in a section of SEM images. The nanoparticle size distribution in Figure 3N was performed using FIJI. The circular cross-section of 15417 nanoparticles was identified by creating binary masks from SEM images using thresholding image segmentation. To remove salt and pepper noise, the despeckle function was used (which is a median filter), followed by "fill holes" and "watershed" functions (to facilitate separate detection of aggregated particles) built-in FIJI. The diameters were calculated from the particle areas calculated using Analyze Particles in FIJI. Micro-particles size distribution in Figure 3N and Figure S12 was calculated by manually measuring the particle diameters for each particle in FIJI for a total of 1697 particles.

To characterize microgel polymeric structures formed during iCVD in different LC templates (Figure 4D-I), we quantified particle shapes by calculating the frequency of appearance of microgel clusters with specific aspect ratio by analyzing SEM images capturing microgels (1087 clusters) formed over a larger grid area using FIJI. Here, Bandpass Filter was used to filter large structures down to 100 pixels and small structures up to 5 pixels to correct for the shadow effect and noise. We then created the binary masks, followed by "fill holes" and "watershed" functions (to facilitate separate detection of aggregated particles) built-in FIJI. The aspect ratio of particles was then calculated from the fitted ellipse mask using the Analyze Particles plug-in in FIJI, as shown in Figure S18 (SEM image, binary mask, mask after processing, and fitted ellipse mask). We then created the weighted frequency plots (weighted by area) using an existing MATLAB function, 'Generate Weighted Histogram' created by Mehmet Suzen (2021) (https://www.mathworks.com/matlabcentral/fileexchange/42493-generate-weighted-histogram), MATLAB Central File Exchange.

We further characterized the directionality of the microgels formed in different LC templates (Figure 4J-O) by analyzing the bright-field optical micrographs obtained over entire grids using FIJI. Here, the binary masks were created using color thresholding after correcting the captured optical micrographs for optimal brightness/contrast and noise (by using a median filter of radius 3), as shown in Figure S19. Directionality histograms were created using the Fourier components method (Nbins = 90) in the directionality plug-in.

A two-sample t-test (with Welch Correction) was performed using Origin (OriginLab, MA) to determine the *p* values in Figures S8, S9 and S15.

References:

1. A. C. Anselmo, S. Mitragotri, Nanoparticles in the clinic. *Bioeng Transl Med* **1**, 10–29 (2016).

2. M. Galia, F. Svec, J. M. J. Frechet, Monodisperse polymer beads as packing material for high-performance liquid chromotography: Effect of divinylbenzene content on the porous and chromatographic properties of poly(styrene-co-divinylbenzene) beads prepared in presence of linear polystyrene as. *J Polym Sci A Polym Chem* **32**, 2169–2175 (1994).

3. T. Ellingsen, O. Aune, J. Ugelstad, S. Hagen, Monosized stationary phases for chromatography. *J Chromatogr A* **535**, 147–161 (1990).

4. B. Yu, C. Tian, H. Cong, T. Xu, Synthesis of monodisperse poly(styrene-co-divinylbenzene) microspheres with binary porous structures and application in high-performance liquid chromatography. *J Mater Sci* **51**, 5240–5251 (2016).

5. Z. Li, H. Zhang, D. Wang, C. Gao, M. Sun, Z. Wu, Q. He, Reconfigurable Assembly of Active Liquid Metal Colloidal Cluster. *Angewandte Chemie - International Edition* **59**, 19884–19888 (2020).

6. K. Deng, Z. Luo, L. Tan, Z. Quan, Self-assembly of anisotropic nanoparticles into functional superstructures. *Chem Soc Rev* **49**, 6002–6038 (2020).

7. J. A. Champion, Y. K. Katare, S. Mitragotri, Particle shape: A new design parameter for micro- and nanoscale drug delivery carriers. *Journal of Controlled Release* **121**, 3–9 (2007).

8. Y. Geng, P. Dalhaimer, S. Cai, R. Tsai, M. Tewari, T. Minko, D. E. Discher, Shape effects of filaments versus spherical particles in flow and drug delivery. *Nat Nanotechnol* **2**, 249–255 (2007).

9. J. Chen, N. E. Clay, N. hyung Park, H. Kong, Non-spherical particles for targeted drug delivery. *Chem Eng Sci* **125**, 20–24 (2015).

10. E. Blanco, H. Shen, M. Ferrari, Principles of nanoparticle design for overcoming biological barriers to drug delivery. *Nat Biotechnol* **33**, 941–951 (2015).

11. S. Mitragotri, J. Lahann, Physical approaches to biomaterial design. *Nat Mater* **8**, 15–23 (2009).

12. P. Kolhar, A. C. Anselmo, V. Gupta, K. Pant, B. Prabhakarpandian, E. Ruoslahti, S. Mitragotri, Using shape effects to target antibody-coated nanoparticles to lung and brain endothelium. *Proc Natl Acad Sci U S A* **110**, 10753–10758 (2013).

13. D. Dendukuri, K. Tsoi, T. A. Hatton, P. S. Doyle, Controlled synthesis of nonspherical microparticles using microfluidics. *Langmuir* **21**, 2113–2116 (2005).

14. H. C. Shum, A. R. Abate, D. Lee, A. R. Studart, B. Wang, C. H. Chen, J. Thiele, R. K. Shah, A. Krummel, D. A. Weitz, Droplet microfluidics for fabrication of non-spherical particles. *Macromol Rapid Commun* **31**, 108–118 (2010).

15. B. Peng, H. R. Vutukuri, A. Van Blaaderen, A. Imhof, Synthesis of fluorescent monodisperse non-spherical dumbbell-like model colloids. *J Mater Chem* **22**, 21893–21900 (2012).

16. W. H. Chen, F. Tu, L. C. Bradley, D. Lee, Shape-Tunable Synthesis of Sub-Micrometer Lens-Shaped Particles via Seeded Emulsion Polymerization. *Chemistry of Materials* **29**, 2685–2688 (2017).

17. J. P. Rolland, B. W. Maynor, L. E. Euliss, A. E. Exner, G. M. Denison, J. M. DeSimone, Direct fabrication and harvesting of monodisperse, shape-specific nanobiomaterials. *J Am Chem Soc* **127**, 10096–10100 (2005).

18. H. Naarmann, N. Theophilou, New process for the production of metal-like, stable polyacetylene. *Synth Met* **22**, 1–8 (1987).

19. Y. Cao, P. Smith, A. J. Heeger, Mechanical and electrical properties of polyacetylene films oriented by tensile drawing. *Polymer (Guildf)* **32**, 1210–1218 (1991).

20. S. Shibahara, M. Yamane, K. Ishikawa, H. Takezoe, Direct Synthesis of Oriented trans-Polyacetylene Films. *Macromolecules* **31**, 3756–3758 (1998).

21. H. Gu, R. Zheng, X. Zhang, B. Xu, Using Soft Lithography to Pattern Highly Oriented Polyacetylene (HOPA) Films via Solventless Polymerization. *Advanced Materials* **16**, 1356–1359 (2004).

22. J. A. Champion, Y. K. Katare, S. Mitragotri, Making polymeric micro- and nanoparticles of complex shapes. *Proc Natl Acad Sci U S A* **104**, 11901–11904 (2007).

23. C. C. Ho, A. Keller, J. A. Odell, R. H. Ottewill, Preparation of monodisperse ellipsoidal polystyrene particles. *Colloid Polym Sci* **271**, 469–479 (1993).

24. S. Guha, A. B. Jindal, An insight into obtaining of non-spherical particles by mechanical stretching of micro- and nanospheres. *J Drug Deliv Sci Technol* **59**, 101860 (2020).

25. K. Li, H. D. H. Stover, Synthesis of Monodisperse Poly(divinylbenzene) Microspheres. *J Polym Sci A Polym Chem* **31**, 3257–3263 (1993).

26. J. S. Downey, R. S. Frank, W.-H. Li, H. D. H. Stöver, Growth Mechanism of Poly(divinylbenzene) Microspheres in Precipitation Polymerization. *Macromolecules* **32**, 2838–2844 (1999).

27. J. S. Downey, G. McIsaac, R. S. Frank, H. D. H. Stöver, Poly(divinylbenzene) Microspheres as an Intermediate Morphology between Microgel, Macrogel, and Coagulum in Cross-Linking Precipitation Polymerization. *Macromolecules* **34**, 4534–4541 (2001).

28. W. H. Li, H. D. H. Stöver, Porous monodisperse poly(divinylbenzene) microspheres by precipitation polymerization. *J Polym Sci A Polym Chem* **36**, 1543–1551 (1998).

29. W. H. Li, H. D. H. Stöver, Monodisperse cross-linked core-shell polymer microspheres by precipitation polymerization. *Macromolecules* **33**, 4354–4360 (2000).

30. E. C. C. Goh, H. D. H. Stöver, Cross-linked poly(methacrylic acid-co-poly(ethylene oxide) methyl ether methacrylate) microspheres and microgels prepared by precipitation polymerization: A morphology study. *Macromolecules* **35**, 9983–9989 (2002).

31. R. S. Frank, J. S. Downey, K. Yu, H. D. H. Stöver, Poly(divinylbenzene-alt-maleic anhydride) microgels: Intermediates to microspheres and macrogels in cross-linking copolymerization. *Macromolecules* **35**, 2728–2735 (2002).

32. K. Li, H. D. H. Stover, Synthesis of Monodisperse Poly (divinylbenzene) Microspheres. *J Polym Sci A Polym Chem* **31**, 3257–3263 (1993).

33. I. Dierking, Polymer Network–Stabilized Liquid Crystals. *Advanced Materials* **12**, 167–181 (2000).

34. C. V. Rajaram, S. D. Hudson, L. C. Chien, Morphology of Polymer-Stabilized Liquid Crystals. *Chemistry of Materials* **7**, 2300–2308 (1995).

35. I. Dierking, L. L. Kosbar, A. Afzali-Ardakani, A. C. Lowe, G. A. Held, Network morphology of polymer stabilized liquid crystals. *Appl Phys Lett* **71**, 2454–2456 (1997).

36. C. V. Rajaram, S. D. Hudson, L. C. Chien, Morphology of diacrylate copolymer networks formed in liquid crystalline media. *Polymer (Guildf)* **39**, 5315–5319 (1998).

37. Y. K. Fung, D. K. Yang, S. Ying, L. C. Chien, S. Zumer, J. W. Doane, Polymer networks formed in liquid crystals. *Liq Cryst* **19**, 797–801 (1995).

38. K. Akagi, Helical Polyacetylene: Asymmetric Polymerization in a Chiral Liquid-Crystal Field. doi: 10.1021/cr900198k.

39. K. C. K. Cheng, M. A. Bedolla-Pantoja, Y. K. Kim, J. V. Gregory, F. Xie, A. De France, C. Hussal, K. Sun, N. L. Abbott, J. Lahann, Templated nanofiber synthesis via chemical vapor polymerization into liquid crystalline films. *Science (1979)* **362**, 804–808 (2018).

40. I. Dierking, Polymer Network–Stabilized Liquid Crystals. *Advanced Materials* **12**, 167–181 (2000).

41. C. V. Rajaram, S. D. Hudson, L. C. Chien, Morphology of Polymer-Stabilized Liquid Crystals. *Chemistry of Materials* **7**, 2300–2308 (1995).

42. I. Dierking, L. L. Kosbar, A. Afzali-Ardakani, A. C. Lowe, G. A. Held, Network morphology of polymer stabilized liquid crystals. *Appl Phys Lett* **71**, 2454–2456 (1997).

43. C. V. Rajaram, S. D. Hudson, L. C. Chien, Morphology of diacrylate copolymer networks formed in liquid crystalline media. *Polymer (Guildf)* **39**, 5315–5319 (1998).

44. Y. K. Fung, D. K. Yang, S. Ying, L. C. Chien, S. Zumer, J. W. Doane, Polymer networks formed in liquid crystals. *Liq Cryst* **19**, 797–801 (1995).

45. J. A. Champion, Y. K. Katare, S. Mitragotri, Particle shape: A new design parameter for micro- and nanoscale drug delivery carriers. *Journal of Controlled Release* **121**, 3–9 (2007).

46. J. Chen, N. E. Clay, N. hyung Park, H. Kong, Non-spherical particles for targeted drug delivery. *Chem Eng Sci* **125**, 20–24 (2015).

47. P. Kolhar, A. C. Anselmo, V. Gupta, K. Pant, B. Prabhakarpandian, E. Ruoslahti, S. Mitragotri, Using shape effects to target antibody-coated nanoparticles to lung and brain endothelium. *Proc Natl Acad Sci U S A* **110**, 10753–10758 (2013).

48. Z. Li, H. Zhang, D. Wang, C. Gao, M. Sun, Z. Wu, Q. He, Reconfigurable Assembly of Active Liquid Metal Colloidal Cluster. *Angewandte Chemie - International Edition* **59**, 19884–19888 (2020).

49. T. J. White, D. J. Broer, Programmable and adaptive mechanics with liquid crystal polymer networks and elastomers. *Nat Mater* **14**, 1087–1098 (2015).

50. M. M. De Luna, P. Karandikar, M. Gupta, Interactions between polymers and liquids during initiated chemical vapor deposition onto liquid substrates. *Mol Syst Des Eng* **5**, 15–21 (2019).

51. L. C. Bradley, M. Gupta, Microstructured Films Formed on Liquid Substrates via Initiated Chemical Vapor Deposition of Cross-Linked Polymers. *Langmuir* **31**, 7999–8005 (2015).

52. A. Bouriche, L. Bedjaoui Alachaher, U. Maschke, Phase behaviour and electro-optical response of systems composed of nematic liquid crystals and poly (2-ethylhexylacrylate). *Liq Cryst* **45**, 656–665 (2018).

53. D. S. Miller, R. J. Carlton, P. C. Mushenheim, N. L. Abbott, Introduction to optical methods for characterizing liquid crystals at interfaces. *Langmuir* **29**, 3154–3169 (2013).

54. J. S. Downey, R. S. Frank, W.-H. Li, H. D. H. Stöver, Growth Mechanism of Poly(divinylbenzene) Microspheres in Precipitation Polymerization. *Macromolecules* **32**, 2838–2844 (1999).

55. C. D. Petruczok, R. Yang, K. K. Gleason, Controllable Cross-Linking of Vapor-Deposited Polymer Thin Films and Impact on Material Properties. *Macromolecules* **46**, 1832–1840 (2013).

56. Q. Yan, T. Zhao, Y. Bai, F. Zhang, W. Yang, Precipitation polymerization in acetic acid: Study of the solvent effect on the morphology of poly(divinylbenzene). *Journal of Physical Chemistry B* **113**, 3008–3014 (2009).

57. H. Jiang, H. Chen, G. Zong, X. Liu, Y. Liang, Z. Tan, Precipitation polymerization in acetonitrile and 1-propanol mixture: Synthesis of monodisperse poly(styrene-co-divinylbenzene) microspheres with clean and smooth surface. *Polym Adv Technol* **22**, 2096–2103 (2011).

58. J. S. Downey, G. McIsaac, R. S. Frank, H. D. H. Stöver, Poly(divinylbenzene) Microspheres as an Intermediate Morphology between Microgel, Macrogel, and Coagulum in Cross-Linking Precipitation Polymerization. *Macromolecules* **34**, 4534–4541 (2001).

59. N. Mac Fhionnlaoich, S. Schrettl, N. B. Tito, Y. Yang, M. Nair, L. A. Serrano, K. Harkness, P. J. Silva, H. Frauenrath, F. Stellacci, S. Guldin, Reversible microscale assembly of nanoparticles driven by the phase transition of a thermotropic liquid crystal. *ChemRxiv* (2017).

60. C. V. Rajaram, S. D. Hudson, L. C. Chien, Effect of Polymerization Temperature on the Morphology and Electrooptic Properties of Polymer-Stabilized Liquid Crystals. *Chemistry of Materials* **8**, 2451–2460 (1996).

61. D. A. Paterson, P. Bao, R. H. Abou-Saleh, S. A. Peyman, J. C. Jones, J. A. T. Sandoe, S. D. Evans, H. F. Gleeson, R. J. Bushby, Control of Director Fields in Phospholipid-Coated Liquid Crystal Droplets. *Langmuir* **36**, 6436–6446 (2020).

62. P. Moni, H. S. Suh, M. Dolejsi, D. H. Kim, A. C. Mohr, P. F. Nealey, K. K. Gleason, Ultrathin and Conformal Initiated Chemical-Vapor-Deposited Layers of Systematically Varied Surface Energy for Controlling the Directed Self-Assembly of Block CoPolymers. *Langmuir* **34**, 4494–4502 (2018).

63. S. Das, N. Atzin, X. Tang, A. Mozaffari, J. de Pablo, N. L. Abbott, Jetting and Droplet Formation Driven by Interfacial Electrohydrodynamic Effects Mediated by Solitons in Liquid Crystals. *Phys Rev Lett* **131**, 098101 (2023).

64. D. S. Seo, K. I. Muroi, T. R. Isogami, H. Matsuda, S. Kobayashi, Polar Anchoring Strength and the Temperature Dependence of Nematic Liquid Crystal (5CB) Aligned on Rubbed Polystyrene Films. *Jpn J Appl Phys* **31**, 2165–2169 (1992).

65. D. Ershov, J. Sprakel, J. Appel, M. A. C. Stuart, J. Van Der Gucht, Capillarity-induced ordering of spherical colloids on an interface with anisotropic curvature. *Proc Natl Acad Sci U S A* **110**, 9220–9224 (2013).

66. I. G. Siny, C. S. Tu, V. H. Schmidt, High Frequency Relaxation in Nematic Liquid Crystal Mixtures by Brillouin Scattering. *Molecular Crystals and Liquid Crystals Science and Technology. Section A. Molecular Crystals and Liquid Crystals* **269**, 125–132 (1995).

67. P. D. Haller, R. J. Frank-Finney, M. Gupta, Vapor-phase free radical polymerization in the presence of an ionic liquid. *Macromolecules* **44**, 2653–2659 (2011).

68. X. Wei, L. C. Bradley, Accessing Thin Film Wetting Regimes during Polymer Growth by Initiated Chemical Vapor Deposition. *Langmuir* **38**, 11550–11556 (2022).

69. K. Ramadhan Makame, M. Sherif, L. Östlundh, J. Sándor, B. Ádám, K. Nagy, Are encapsulated pesticides less harmful to human health than their conventional alternatives? Protocol for a systematic review of in vitro and in vivo animal model studies. *Environ Int* **174** (2023).

70. L. Corrêa-Filho, M. Moldão-Martins, V. Alves, Advances in the Application of Microcapsules as Carriers of Functional Compounds for Food Products. *Applied Sciences* **9**, 571 (2019).

71. K. Unger, P. Salzmann, C. Masciullo, M. Cecchini, G. Koller, A. M. Coclite, Novel Light-Responsive Biocompatible Hydrogels Produced by Initiated Chemical Vapor Deposition. *ACS Appl Mater Interfaces* **9**, 17408–17416 (2017).

72. R. K. Bose, K. K. S. Lau, Initiated CVD of poly(2-hydroxyethyl methacrylate) hydrogels: Synthesis, characterization and in-vitro biocompatibility. *Chemical Vapor Deposition* **15**, 150–155 (2009).

73. W. Reichstein, L. Sommer, S. Veziroglu, S. Sayin, S. Schröder, Y. K. Mishra, E. İ. Saygili, F. Karayürek, Y. Açil, J. Wiltfang, A. Gülses, F. Faupel, O. C. Aktas, Initiated chemical vapor deposition (Icvd) functionalized polylactic acid–marine algae composite patch for bone tissue engineering. *Polymers (Basel)* **13**, 1–11 (2021).

74. A. Fasanella, M. Castriota, E. Cazzanelli, L. De Sio, R. Caputo, C. Umeton, Molecular Orientation of E7 Liquid Crystal in POLICRYPS Holographic Gratings: A Micro-Raman Spectroscopic Analysis. *Molecular Crystals and Liquid Crystals* **558**, 46–53 (2012).

75. M. Castriota, A. Fasanella, E. Cazzanelli, L. De Sio, R. Caputo, C. Umeton, In situ polarized micro-Raman investigation of periodic structures realized in liquid-crystalline composite materials. *Opt Express* **19**, 10494 (2011).

76. E. V. Astrova, T. S. Perova, S. A. Grudinkin, V. A. Tolmachev, Y. A. Pilyugina, V. B. Voronkov, J. K. Vij, Polarized infrared and Raman spectroscopy studies of the liquid crystal E7 alignment in composites based on grooved silicon. *Semiconductors* **39**, 759–767 (2005).

77. C. H. Hung, B. Singh, M. G. Landowski, M. Ibrahim, A. J. Miles, D. S. Jensen, M. A. Vail, A. E. Dadson, S. J. Smith, M. R. Linford, Multi-instrument characterization of poly(divinylbenzene) microspheres for use in liquid chromatography: As received, air oxidized, carbonized, and acid treated. *Surface and Interface Analysis* **47**, 815–823 (2015).

78. E. Partouche, S. Margel, Carbonization of PAN grafted uniform crosslinked polystyrene microspheres. *Carbon N Y* **46**, 796–805 (2008).

79. K. Araya, K. Iwasaki, Solubility parameters of liquid crystals. *Molecular Crystals and Liquid Crystals Science and Technology Section A: Molecular Crystals and Liquid Crystals* **392**, 49–57 (2002).

80. M. P. Neto, J. A. Castanharo, M. G. De Oliveira, M. A. Da SilvaCosta, Influence of the fraction of comonomers and diluents on the preparation of polymeric microspheres based on poly (methacrylic acid-co-divinylbenzene) obtained by precipitation polymerization. *Materials Research* **22** (2019).

81. M. Tamizifar, G. Sun, Control of surface radical graft polymerization on polyester fibers by using Hansen solubility parameters as a measurement of the affinity of chemicals to materials. *RSC Adv* **7**, 13299–13303 (2017).

82. R. J. Frank-Finney, L. C. Bradley, M. Gupta, Formation of polymer-ionic liquid gels using vapor phase precursors. *Macromolecules* **46**, 6852–6857 (2013).

83. P. D. Haller, L. C. Bradley, M. Gupta, Effect of surface tension, viscosity, and process conditions on polymer morphology deposited at the liquid-vapor interface. *Langmuir* **29**, 11640–11645 (2013).

84. L. C. Bradley, M. Gupta, Formation of Heterogeneous Polymer Films via Simultaneous or Sequential Depositions of Soluble and Insoluble Monomers onto Ionic Liquids. *Langmuir* **29**, 10448–10454 (2013).

85. L. C. Bradley, M. Gupta, Encapsulation of ionic liquids within polymer shells via vapor phase deposition. *Langmuir* **28**, 10276–10280 (2012).

86. R. J. Frank-Finney, P. D. Haller, M. Gupta, Ultrathin free-standing polymer films deposited onto patterned ionic liquids and silicone oil. *Macromolecules* **45**, 165–170 (2012).

87. P. D. Haller, M. Gupta, Synthesis of polymer nanoparticles via vapor phase deposition onto liquid substrates. *Macromol Rapid Commun* **35**, 2000–2004 (2014).

88. P. Karandikar, M. Gupta, Synthesis of Functional Particles by Condensation and Polymerization of Monomer Droplets in Silicone Oils. *Langmuir* **33**, 7701–7707 (2017).

89. E. Bukusoglu, M. B. Pantoja, P. C. Mushenheim, X. Wang, N. L. Abbott, Design of Responsive and Active (Soft) Materials Using Liquid Crystals. *Annu Rev Chem Biomol Eng* **7**, 163–196 (2016).

Acknowledgments

AJ acknowledges Danielle Streever for her help with generating microspheroid size distribution from collected data and Philip Carubia for his help with optimizing Raman spectral acquisition conditions.

Funding: This material is based upon work supported by the National Science Foundation (NSF) through the Future Manufacturing Research Grant under Grant No. CMMI-2229092 and through the Faculty Early Career Development Program under Grant No. CMMI-2144171. Analytical methods involved the use of the Cornell Center for Materials Research (CCMR) Shared Facilities, which are supported by the NSF MRSEC program (DMR-1719875).

Author contributions: AJ and SP conducted the experiments and analyzed the data. All authors discussed the results and the interpretation. NLA and RY conceived and directed the study. AJ, SP, NLA, and RY discussed the results and the interpretation and composed and revised the manuscript.

Competing interests: AJ, SP, NLA, and RY are inventors of a pending international patent application No. PCT/US2023/066722 filed May 8, 2023. The authors declare no other competing interests.

Data and materials availability: All data needed to evaluate the conclusions in the paper are present in the paper and/or the Supplementary Materials.

Supporting Information

***Supporting Movies**:*

Movie S1 (.mp4 format). Nematic to Isotropic transition above threshold monomer partial pressure

Movie S2 (.mp4 format). Real-time monitoring of 90 minutes of polymerization on rubbed-PI substrate (in cross-polarized mode)

Movie S3 (.mp4 format). LC alignment change from planar to homeotropic on glass due to lowering of surface energy

Movie S4 (.mp4 format). In-situ polymerization observation (in bright-field mode) capturing shape transition for 60 minutes of polymerization on rubbed-PI substrate

Supplementary Figures:

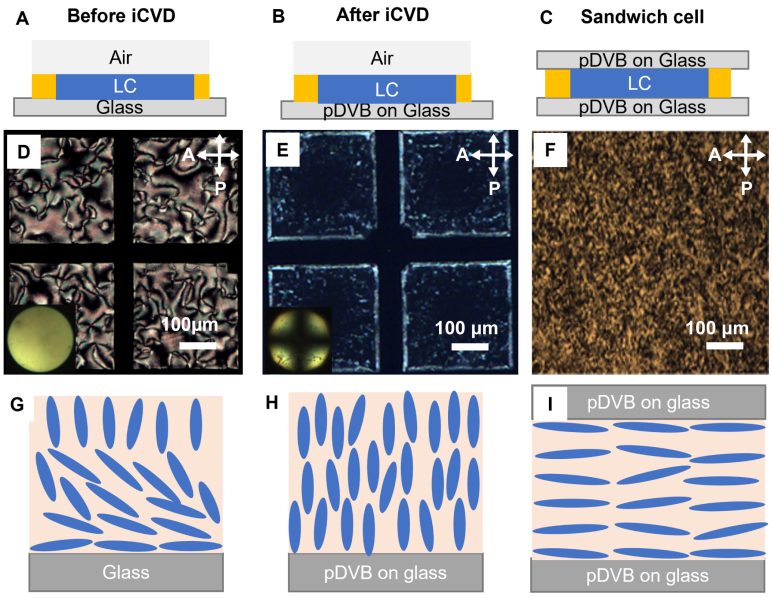

Figure S1. Investigating the mechanism of LC anchoring transition. Schematic of the experimental setup (A-C), their corresponding orthoscopic and conoscopic (insets) cross polarized optical micrographs (D-F) and the corresponding schematics of LC molecular orientation in each system (G-I).

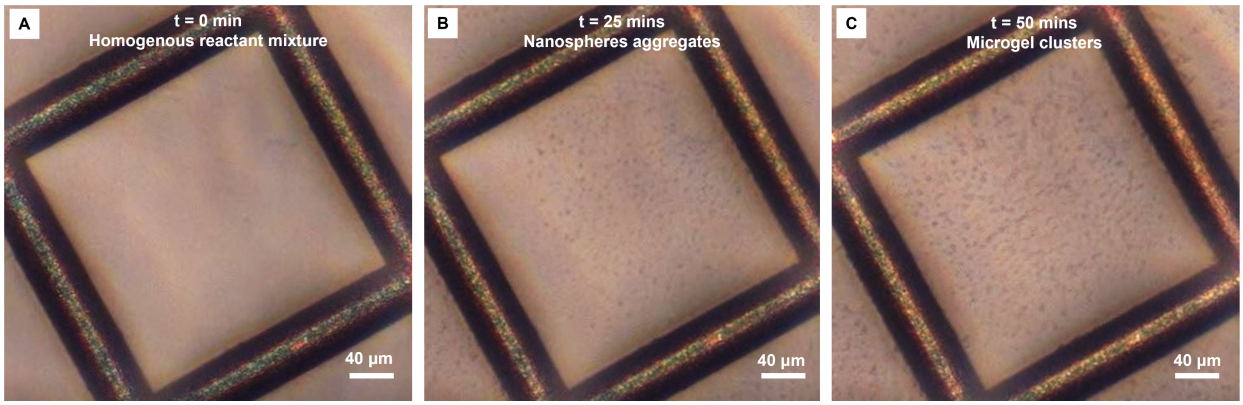

Figure S2. Time progression of shaped polymeric structures from real-time monitoring of iCVD polymerization for 60 mins. Snapshots taken from in-situ observation in bright-field mode (see Movie S4 for video) captures the progression of reaction from homogenous reactant mixture at the start (A), to observation of nanospheres at 25 minutes (B) and, formation of elongated microgel clusters from nanospheres at 50 minutes (C).

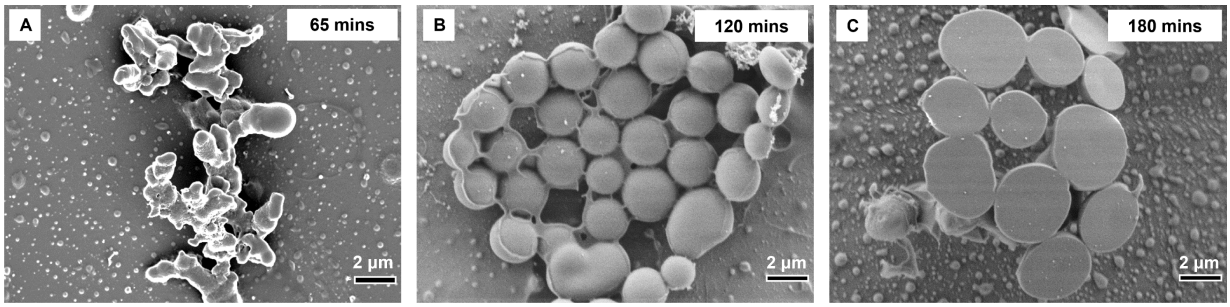

Figure S3. Polymeric shapes obtained after removal of LC using CPD coincides with the observed shapes after ethanol washing. Representative SEM images captures the microgel clusters formed after 65 minutes of polymerization (A) and, micron-sized spheroids formed after 120 and 180 minutes of polymerization at LC-substrate interface (B-C).

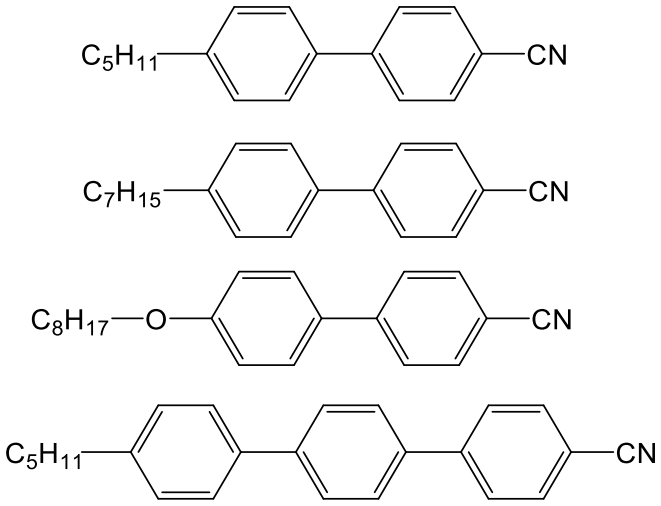

Figure S4. Molecular structure for constituents of E7 LC mixture.

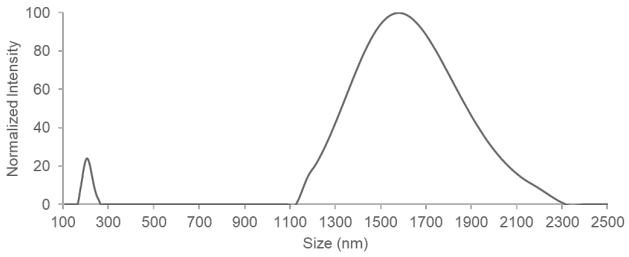

Figure S5. Size distribution of nanospheres and microgels obtained at the end of 65 minutes of polymerization using DLS.

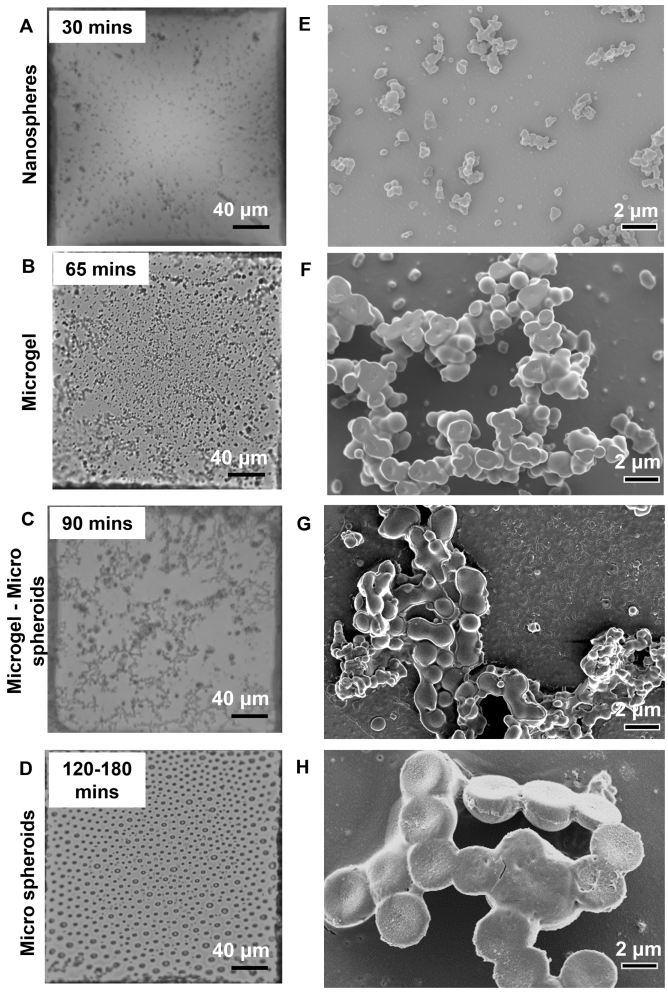

Figure S6. Morphology progression of the pDVB particles from nanospheres to microgel clusters to micron-sized spheres, spheroids, and discs over time during the iCVD in LC process on glass substrate. (**A-D**) Ex-situ bright field optical micrographs capturing the formation of polymer structures (dark clusters) over one complete grid of LC medium, (**E-H**) Representative SEM images capturing the detailed shapes of the polymer particles formed at the LC-substrate interface. The presence of nanospheres at all times illustrates their continuous precipitation.

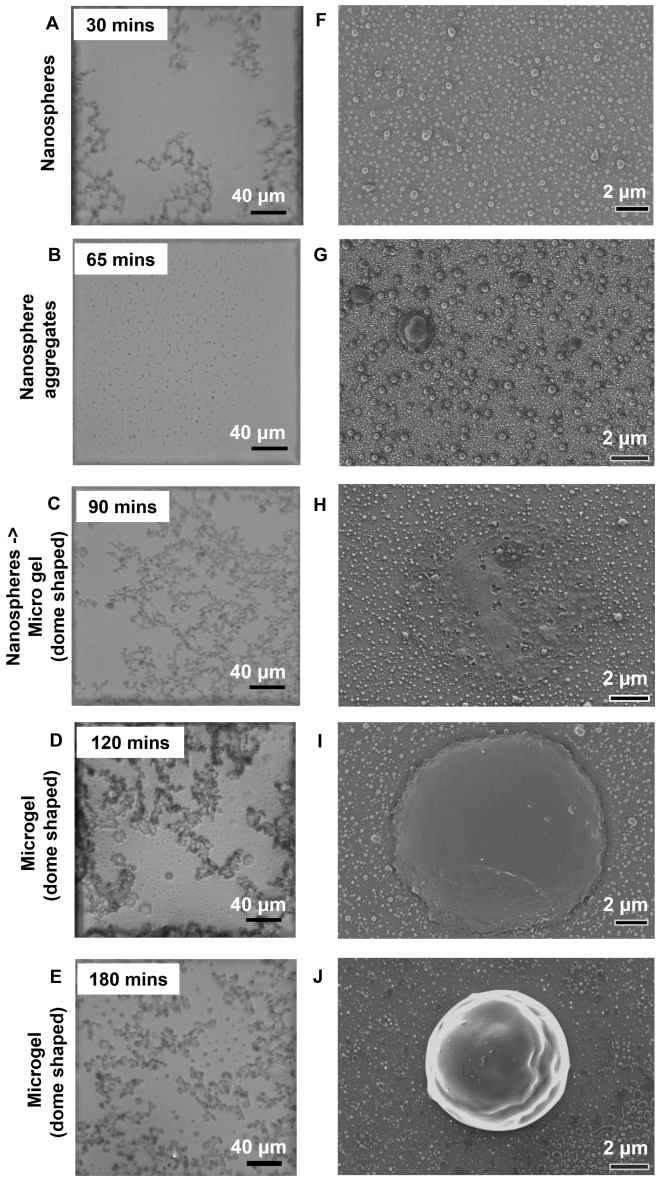

Figure S7. Morphology progression of the pDVB particles from nanospheres to microgel clusters (dome-shaped) over time during the iCVD in LC process on OTS substrate. (A-D) Ex-situ bright field optical micrographs capturing the formation of polymer structures (dark clusters) over one complete grid of LC medium, (**E-H**) Representative SEM images capturing the detailed shapes of the polymer particles formed at the LC-substrate interface. The presence of nanospheres at all times illustrates their continuous precipitation. Shape progression for polymerization on OTS substrate was observed to be slower than the other two substrates.

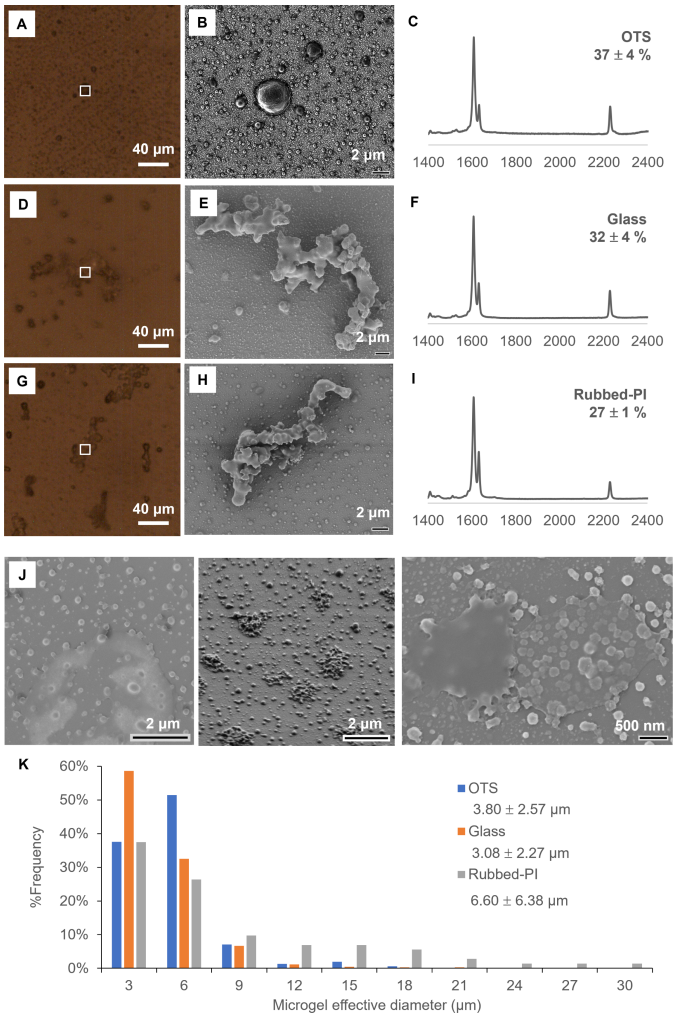

Figure S8. Properties of microgel clusters formed in LC on OTS, glass, and rubbed-PI substrates. Representative Raman microscopy images, corresponding SEM images, Raman spectra and % vinyl bonds left unreacted characterized for microgel clusters formed in OTS (A-C), glass (D-F) and rubbed-PI (G-I) LC templates, respectively. The difference in % unreacted vinyl bonds are statistically not significant between OTS and glass (with $p = 0.129$), not significant between glass and rubbed-PI (with $p = 0.094$) but is significant between OTS and rubbed-PI (with $p = 0.0066$). The observed difference is likely due to difference in diffusion coefficients in x-y plane (owing to different mesogenic alignments) which results in different rates of aggregation of nanospheres (slower in OTS) than heterogenous polymerization, resulting in higher % unreacted vinyl bonds in OTS. (J) SEM images indicative of mechanism

of simultaneous aggregation of precipitated nanospheres and heterogenous polymerization. (K) Microgel effective particle size distribution for a microgel population formed after 65 minutes of polymerization in LC on OTS functionalized glass, glass and, rubbed-PI functionalized glass respectively.

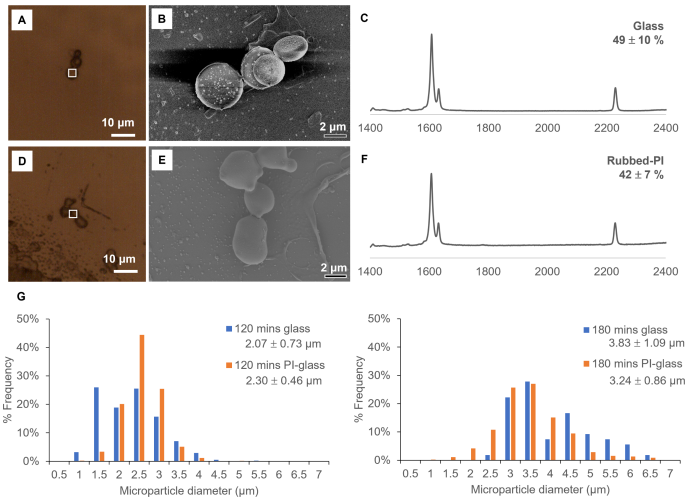

Figure S9. Properties of microparticles formed in LC on glass and rubbed-PI substrates. Representative Raman microscopy images, corresponding SEM images, Raman spectra and % vinyl bonds left unreacted characterized for particles formed in glass (A-C) and, rubbed-PI (D-F) LC templates, respectively. The % unreacted vinyl bonds are not statistically different (with $p = 0.295$). (G) Particle size distribution for particles formed after 120 and 180 minutes of polymerization in LC on glass and rubbed-PI functionalized glass, respectively.

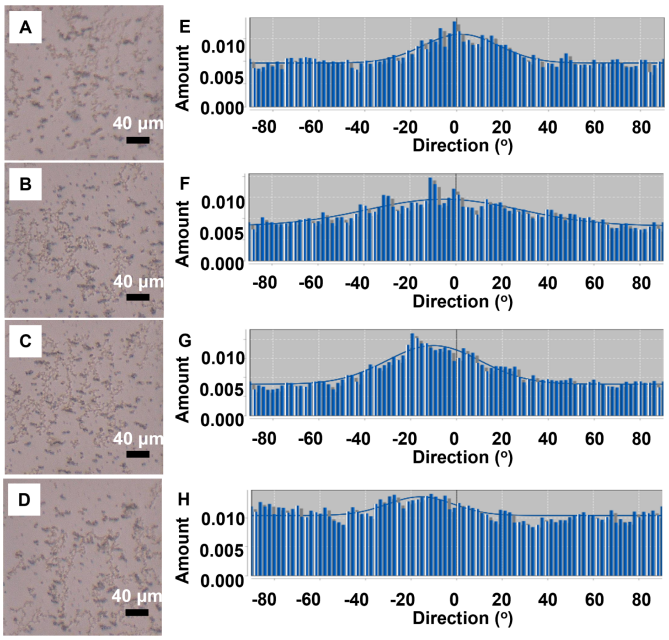

Figure S10. Bulk alignment of microgels on rubbed PI-functionalized substrates. Bright-field optical micrographs of several grids captured over a length scale of 3.05 mm (A-D) and corresponding directionality histograms (E-H) of the polymeric clusters highlight the presumed direction of rubbing on the substrate.

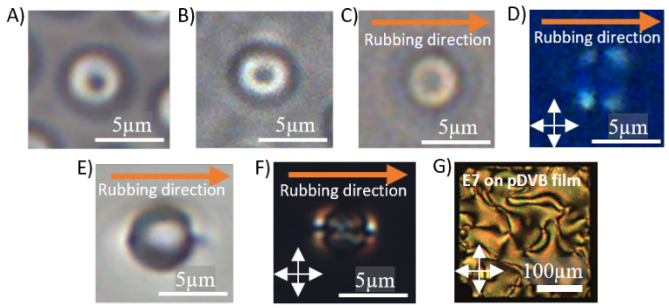

Figure S11. Weak tangential anchoring of LC on the surface of pDVB microparticle synthesized by iCVD-in-LC. A)-B) Bright-field optical images of a microspheroid formed in nematic E7 on an OTS-functionalized glass surface showing a dark dot-like optical feature A) above and B) below the microspheroid (inferred by inverting the substrate supporting the LC and microspheroids and imaging above the particles) . C)-D) Optical micrographs of a microspheroid dispersed in LC hosted between two confining rubbed PI surfaces C) using brightfield imaging and D) under crossed polarizers, with the latter showing the presence of optical lobes around the particle consistent with tangential anchoring of LC on the microspheroid. E)-F) Optical micrographs of a commercially sourced PS microparticle (known to induce tangential anchoring of LC around the particle) that was dispersed in LC hosted between two rubbed PI surfaces E) using brightfield imaging and F) under crossed polarizers, both showing the evidence of Boojum defects. G) Cross polarized optical micrograph of a film of nematic E7 on a pDVB film (synthesized by iCVD on a glass surface without LC) showing tangential anchoring of E7 on the film.

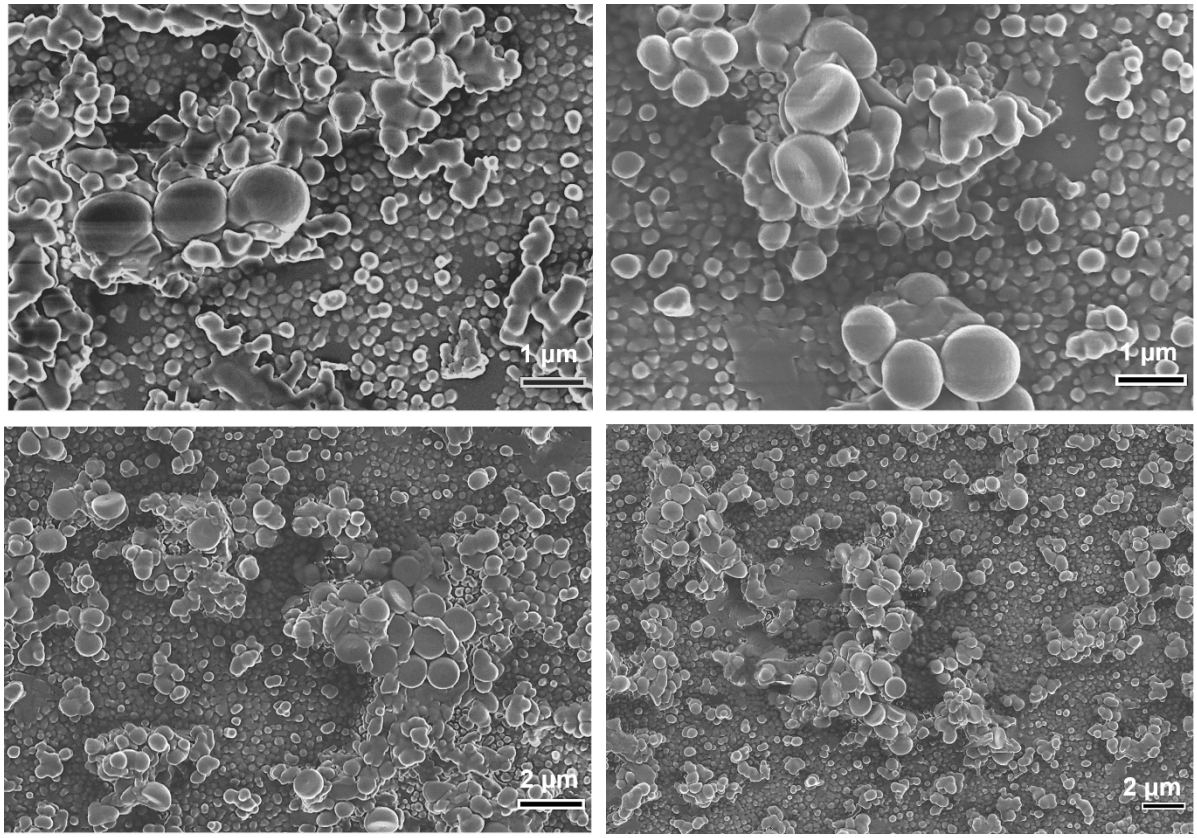

Figure S12. Representative SEM images capturing the transition of nanoscopic assembly to emergence of microparticles at the LC-substrate interface on glass coated with polyimide after 90 minutes of iCVD polymerization.

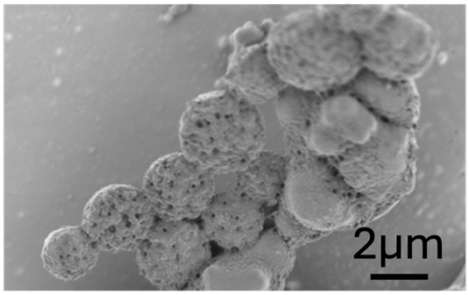

Figure S13. The emergence of microspheroids from a collection of nanospheres on glass substrates.

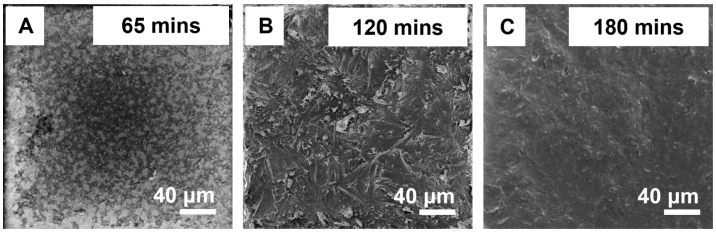

Figure S14. Film formation at LC-vapor interface. Partial film coverage was observed for polymerization till 65 minutes (A), and porous film formation was observed for longer reaction times i.e 120 minutes (B) and 180 minutes (C). Note that, to capture the film structure formed on LC-vapor interface at top for SEM imaging, in these experiments LC was removed by vacuum drying for 1 day at 75^{o}C.

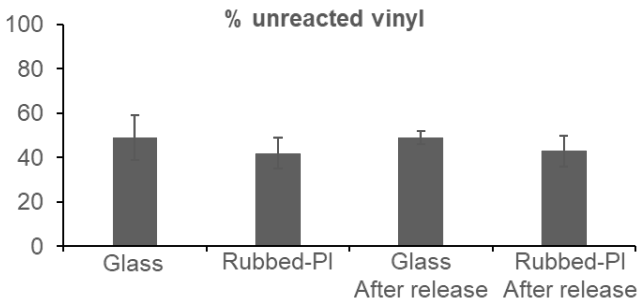

Figure S15. Percentage unreacted vinyl bonds present in microparticles before and after LC release for particles formed over glass (p = 0.882) and rubbed-PI (p = 0.851).

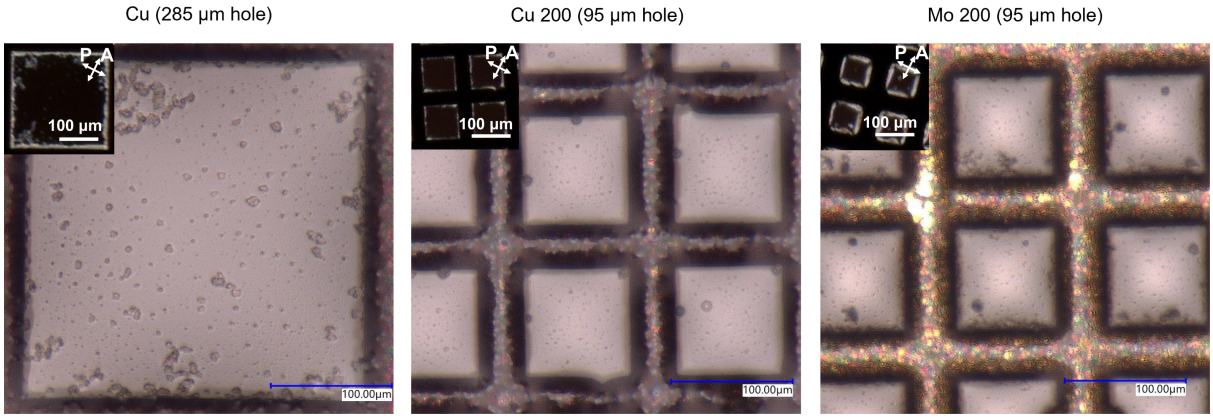

Figure S16. Polymer morphology for synthesis performed in LC flat films formed using different TEM grids at monomer partial pressure (26 mTorr) for 65 minutes on OTS functionalized substrate. Using TEM grids with different composition or dimensions do not affect the polymerization process as shown from the observed polymeric structures formed after iCVD in LC film formed using copper and molybdenum TEM grids with dimensions of 285 µm x 285 µm and 95 µm x 95 µm. Insets are cross polarized micrographs corresponding to homeotropic (perpendicular) alignment of LC molecules on OTS functionalized substrate in each variant of TEM grid after polymerization.

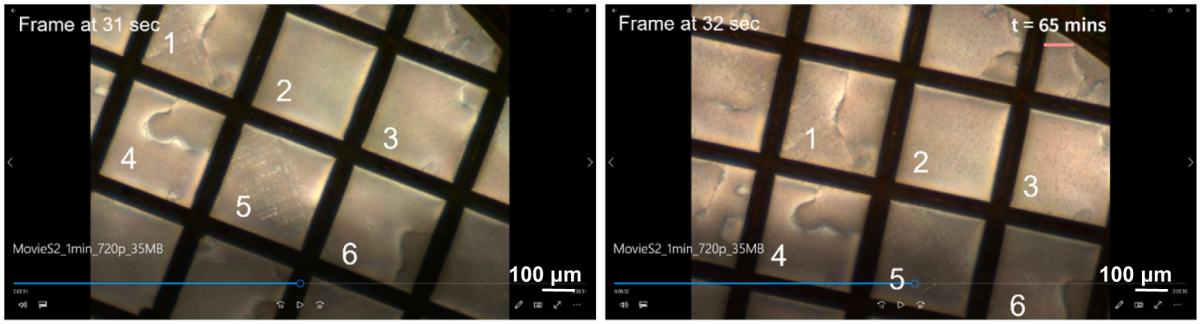

Figure S17. In-situ microscope images at 31s and 32s of Movie S2, highlighting a slight frame switch due to microscope handling. The six grids that were monitored in real-time are labeled.

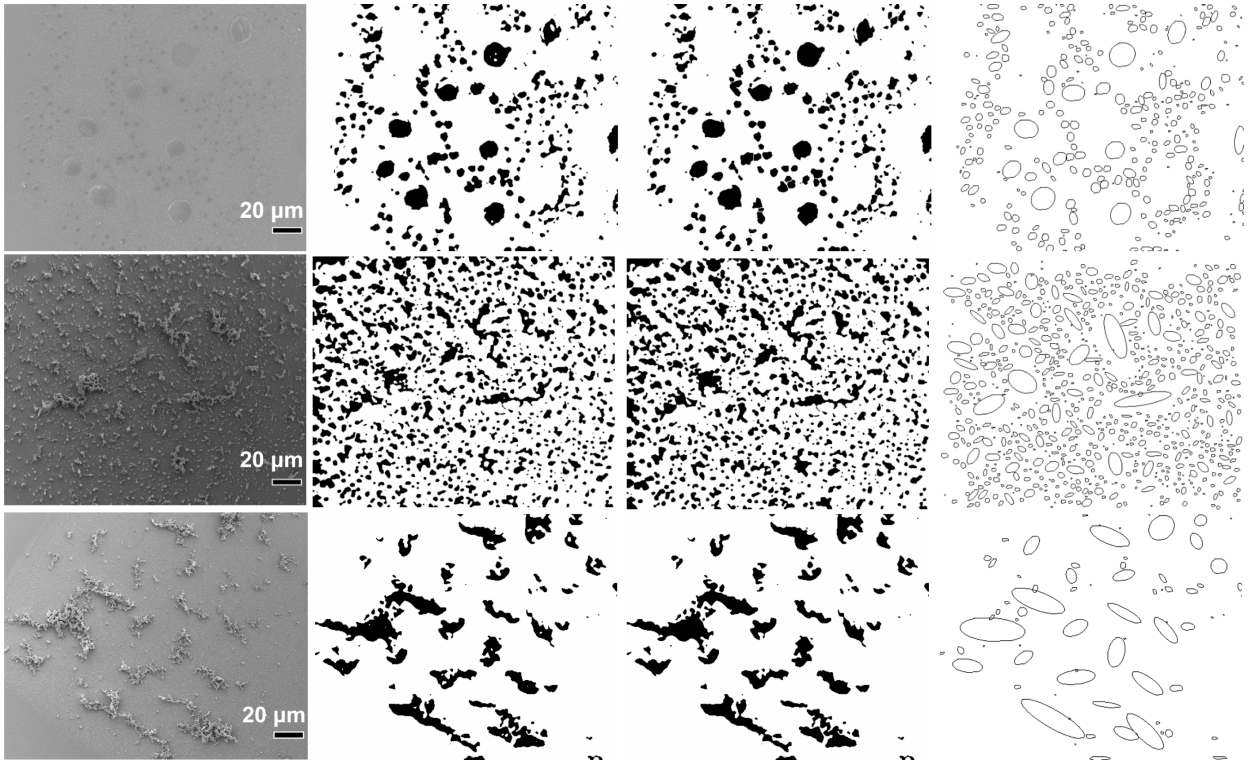

Figure S18. Characterization of microgel particles shape. Methodology used for creation of binary masks from SEM images for calculation of particles aspect ratio.

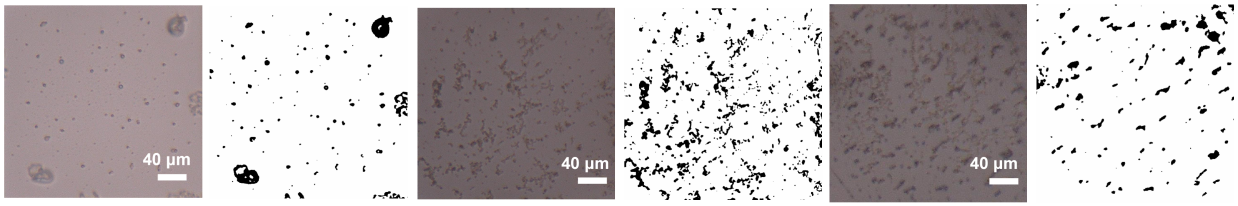

Figure S19. Characterization of microgel particles directionality. Binary masks creation from bright-field optical micrographs of an entire grid for plotting particles directionality histograms.

Supplementary Tables

Table S1: **iCVD reaction conditions**

P_{DVB} mTorr	P_{TBPO} mTorr	P_{Ar} mTorr	T_{Stage} ^0C	Time mins	LC Phase	LC orientation	Particle shape
26.9	3.8	119.2	20	30	Nematic	Homeotropic & Hybrid	Nanoparticles
26.9	3.8	119.2	20	65	Nematic	Homeotropic	Hemispherical dome shaped
26.9	3.8	119.2	20	65	Nematic	Hybrid (random in-plane	Random elongated clusters
26.9	3.8	119.2	20	65	Nematic	Hybrid (directional in-plane)	Oriented elongated clusters
26.9	3.8	119.2	20	120-180	Nematic	Homeotropic & Hybrid	Microparticles

Table S2: Reactor conditions to probe for LC structure disruptions during iCVD

Species	Partial Pressure (mTorr)	Stage Temperature (^{0}C)	LC Phase
DVB	7.7 – 26.9	20	Nematic
DVB	30.5 – 46.1	20	Isotropic
TBPO	3.8 – 90	20	Nematic
Argon	101.9 – 150	20	Nematic

Table S3: LC substrates in figures

Substrate	Figure number	Data type
Glass	2A	In-situ cross-polarized OM
PI-functionalized glass	2B	In-situ cross-polarized OM
Glass	2C	In-situ cross-polarized OM
PI-functionalized glass	3A-D, E-H	Ex-situ bright-field OM, SEM
PI-functionalized glass	3K-M*	Raman microscopy images & spectra
OTS-functionalized glass	4A, D, J	Ex-situ cross-polarized OM, SEM, Ex-situ bright-field OM
Glass	4B, E, K	Ex-situ cross-polarized OM, SEM, Ex-situ bright-field OM
PI-functionalized glass	4C, F, L	Ex-situ cross-polarized OM, SEM, Ex-situ bright-field OM
Glass	S1	Ex-situ cross-polarized OM
PI-functionalized glass	S2	In-situ bright-field OM
PI-functionalized glass	S3	SEM
PI-functionalized glass	S5	DLS
OTS-functionalized glass	S6	SEM
OTS-functionalized glass	S7A-E, F-J	Ex-situ bright-field OM, SEM
Glass	S8A-D, E-H	Ex-situ bright-field OM, SEM
OTS-functionalized glass	S9A-C	Raman microscopy, SEM, spectra
Glass	S9D-F	Raman microscopy, SEM, spectra
PI-functionalized glass	S9G-I	Raman microscopy, SEM, spectra
Glass	S10A-C	Raman microscopy, SEM, spectra

PI-functionalized glass	S10D-F	Raman microscopy, SEM, spectra
PI-functionalized glass	S11A-D	Ex-situ bright-field OM

*Representative spectra shown were captured on PI-functionalized glass, however, the unreacted vinyl% were calculated using data collected on all substrates

1. Reactant concentrations in LC

Under the conditions used in this report, the partitioning of TBO radicals into LC is expected to be lower than DVB monomer owing to (*i*) the lower partial pressure of 3.8 mTorr of TBO as compared to 26.9 mTorr of DVB in the vapor phase, and (*ii*) the lower solubility and hence Henry's coefficient of TBO than DVB in LC. The latter was estimated using the Hildebrand solubility parameter, δ. The closer the δ values, the more soluble the two chemicals are expected to be. It has been reported that δ for LC is ~ 21.5 $Mpa^{1/2}$ (*67*), δ for DVB is ~ 19.9 $Mpa^{1/2}$ (*68*), and δ for TBPO (i.e., the precursor to TBO radicals) is ~ 16.7 $Mpa^{1/2}$*(69*). DVB is therefore expected to be more soluble in LC than TBO radicals.

2. Polymer shapes obtained in iCVD polymerization in isotropic liquids

The iCVD synthesis in isotropic liquids has been studied extensively in the last decade (4*0, 41 55, 70-75*). It has been shown to form polymer morphologies such as nanoparticles, films, and gels based on the choice of monomers and liquids for tuning parameters such as surface tension, viscosity, and solubility (*40*). In the cases of nanoparticles synthesis, they were formed at a vapor-liquid interface driven by polymer aggregation into particles due to a negative spreading coefficient and insolubility of monomers like n-butyl acrylate and 4-vinylpyridine in liquid reaction mediums such as polydimethylsiloxane and krytox (*75*). Another strategy to synthesize nanoparticles using iCVD was polymerizing condensed monomer droplets onto liquid substrates (*76*). Both strategies synthesized particles on top of the substrates, in contrast to precipitating nanoparticles inside the LC medium obtained in this work. For crosslinking monomers like DVB, iCVD polymerization in isotropic liquids has been shown to form micro-structured films (*41*), thus distinct from the particles obtained in this work. We believe the morphological evolution is a distinct outcome of the nematic structure of the LC, which guided

the precipitation of the insoluble pDVB nanoparticles and their assembly at the LC-substrate interface. The pDVB nanoparticles in turn served as building blocks for the microstructures.

3. Liquid Crystals (LC) – what happens when a particle is introduced in an LC nematic host

When a particle is present inside LC, LC molecules in the vicinity of the particle surface will deviate from the bulk director (i.e., long range order of LC medium) to minimize the resulting elastic strain while simultaneously satisfying anchoring conditions at the particle surface in addition to the confining boundaries of LC. The energy associated with elastic distortions of LC away from the bulk director near the particle surface is defined as κr, where κ is the average Frank elastic constant for splay and bend of the LC and r is the radius of the particle inclusion. The interfacial energy associated with the interaction of LC with the particle surface has an additional orientation-dependent component estimated as Wr^2, where W is the surface anchoring energy density. As such, extrapolation length ξ is defined as $\frac{\kappa}{W}$, such that if particle size exceeds the extrapolation length, it is favorable for LC to deform around the particle inclusion while for particles smaller than ξ, it is energetically favorable for LC molecules to remain along the bulk director (77).